NUS

National University
of Singapore

EE4001 Honour's year dissertation in partial fulfillment of the requirements for the Degree of Bachelor of Engineering
Academic Year 2008/2009
Supervisor (ECE): Dr. Aaron Danner
Supervisor (CQT): Dr. Antía Lamas-Linares
Examiner: Dr. Daniel Pickard
Supervisee & Examinee: Mai Lijian (U066874H)

Contents

1 Introduction

As classical information technology reaches its limits due to unsustainable device miniaturization or theoretical upper bounds imposed by classical information theory (e.g. Shannon's information entropy), new methods for realizing fast and secure information processing and communication are needed to meet ever increasing demand for information processing speed and security. Quantum information technology is a possible candidate to meet this challenge by using quantum physics to do what classical physics cannot. However, just like classical information theory, which uses bits as its basic unit of information, quantum information theory relies on quantum-bits, or "qubits", as its fundamental unit of information. Ever since the first ground breaking works on quantum cryptography [1, 2] were published, the photon has always touted as the ideal candidate to play the role of the "flying qubit" [3]; that is, an entity to carry information between quantum information systems, much like a train of electronic pulses carry bits in today's electronic systems. It is predominantly for this purpose that many schemes [3] have been devised to generate such single photons. However, each of these schemes suffer from deficiencies that still restrains them from being true, deterministic and ideal single photon sources. Take for example, the workhorse of quantum cryptography [3, 4, 5], spontaneous parametric down conversion sources. These sources suffer from low brightness and does not give a photon on demand [4]. Also, measuring the photon statistics over a long time window will reveal that it is not a true single photon source [3]; measuring of these photon statistics will be discussed in section 2.1.2. Thus, creating true single photon sources are not trivial and is an area of intense research [3].

Photons, by being a type of Boson [6] (particles which adhere to the Bose-Einstein statistics) exhibit a property known as "Bosonic Bunching", or simply, "Bunching"; in which several photons of the same mode, tend to spatially coalesce together should they meet [7]. Thus, when the term "single photons" is invoked, they actually mean photons that are in an "anti-bunched" state, that is, spatially separated from one another and not bunched together. These aforementioned terms shall be used interchangeably hereafter in this thesis to mean anti-bunched single photons. Photon anti-bunching is a completely quantum mechanical phenomena and cannot be explained or predicted by classical theories of light [8]; its manifestation involves the explanation of light in terms of corpuscular photons. In classical theory, light can be continuously divided in irradiance into halves.

Fluorescence from a single molecule is one of the few schemes proposed where single photons have been detected [3]. This is possible as fluorescing molecules in solid state matrices can absorb and emit only a single photon at a time through a turnstile excitation and de-excitation cycle. However, these emissions are not on-demand, as would be desired in a reliable and deterministic communication device. To achieve an on demand emission, such a molecule can be triggered by a pulsed excitation scheme [9]. But even then, the probability of having only one photon and not any other number is less than 90%.

In this thesis, a scheme using a laser scanning confocal microscope to observe photon anti-bunching will be discussed. The molecules are simply low concentrations of fluorescent dyes which will be placed on a coverslip, which is a thin sheet of glass, and put under the microscope for observation. The molecules will be held in place on the coverslip by a layer of solid host matrix. Methods of creating a sample that is suitable for these experiments will also be discussed, including coverslip cleaning, spin-coating and sample preparation.

An inherited confocal setup is enhanced in my project and will be characterized in the chapters that follow. This microscope is equipped to be single photon sensitive and has a spectrum analyzing tool (hereafter, the spectrometer). The spectrometer will allow any light to be converted into its optical spectrum. To verify the anti-bunching of detected light, a Hanbury Brown and Twiss setup is also included to measure a set of photon statistics from which the anti-bunching status can be ascertained. I will also touch on the aligning methods of the microscope and all its detection attachments (both the spectrometer and the Hanbury Brown and Twiss setup).The experimental setup allows flexible adaptation to other wavelength or emitters, e.g. to single colour-centers in diamond [10, 11].

Such setups have already been demonstrated before and are well documented in literature [9, 10, 11, 12, 13, 14, 15, 16]. But these experiments, with the exception of [12, 13] have always been carried out with laser beams and coherent lighting. This experiment will attempt to replace these lasers by incoherent light sources in the form of inexpensive, commercially available light emitting diodes. Recent advances in solid state lighting has brought about a ready market of high brightness LEDs and in this thesis I will summarize the efforts undertaken to use these LEDs as an illumination scheme for such experiments. Pertinent topics include spectral and spatial filtering of incoherent light, characterization of light that is being focused onto a sample and results of this experiment.

Lastly, I shall also conclude with an outlook section in which future steps that can be taken with the research *status quo* are duly discussed.

2 Theory

In this chapter, theoretical concepts which are used in the experiments are reviewed. The emission characteristics of molecules will be discussed, followed by techniques to detect photon anti-bunching. As microscopy is extensively used, basic elements of microscopy will be reviewed. Lastly, as LEDs are also used in this experiment, a short section on colourimetry will be presented; covering conversion between photometric units, which are often used in the LED literature, and radiometric units, which is used in the experiment.

2.1 Quantum optics

Whereas classical optics would have it that light is an electromagnetic wave, quantum optics analyzes light by modeling it as discrete photons. Both theories would give predictions on light that are, in some cases, complementary and in other cases, contradictory. In this experiment, the quantum optical nature of light emitted by a single molecule acting as a quantum emitter is investigated. In this section, the basic theories of quantum optics pertaining to the experiment will be reviewed.

2.1.1 Quantum emitters and molecular fluorescence

Quantum emitters are nano-sized structures that are quantum confined systems; i.e. small objects where the number of atoms are sufficiently small enough for the quantum nature to become dominant as the ensemble behavior diminishes. Quantum emitters can be approximated as a two level system [17], that is, by considering only 2 energy levels that have an energy difference that is within the range of the excitation photon energy. In a fluorescent molecule, these two levels are often referred to HOMO and LUMO energy levels in literature [17]. With HOMO being the abbreviation for "highest occupied molecular orbital and LUMO being the abbreviation for "lowest unoccupied molecular orbital". Also for a fluorescent molecule, a third state is also present with an energy level that is between the HOMO and LUMO states. This is the triplet state, denoted as $|\mathrm{T}_1\rangle$ on a Jabłonski energy diagram in Figure 1. Whereas the HOMO and LUMO states are singlet states, denoted as $|\mathrm{S}_1\rangle$ and $|\mathrm{S}_0\rangle$ in Figure 1.

From Figure 1, it is evident that the excitation photon is able to excite an electron into any one of the vibrational states of $|S_1\rangle$. The possibility of excitation into any of these finely spaced level is what gives the absorption spectrum its broad profile (see Figure 2), despite the singlet states having discrete energy levels. The converse is also true for emission; the ability for the electron to relax into any of the finely spaced energy levels of $|S_0\rangle$ explains its broad emission spectrum. After excitation, the electron typically relaxes into the least energetic level of $|S_1\rangle$ in a non-radiative decay before finally relaxing back into $|S_0\rangle$. The non-radiative decay that occurs within $|S_1\rangle$ results in the emitted photon having less energy and larger wavelength compared to the excitation photon. This accounts for a shift between the absorption and emission spectrums of the molecule. The difference between the dominant absorption and emission wavelengths is known as the Stokes shift and is shown in Figure 2. The value of the Stoke's

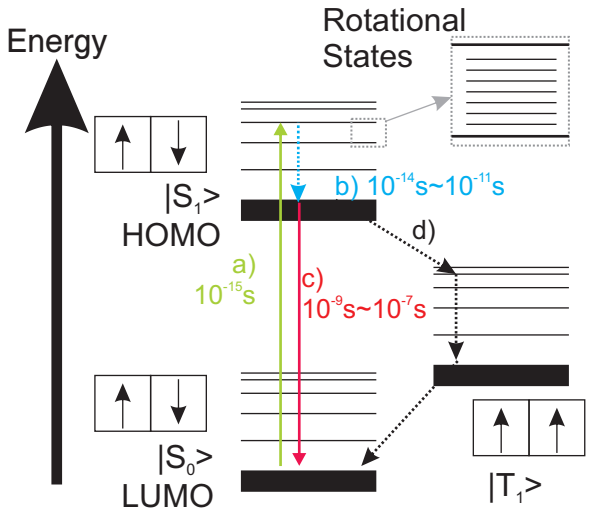

Figure 1: Jabłonski energy diagram [18, 19], S denotes singlet states, and T denotes the triplet state. (a) denotes an excitation event, (b) denotes non-radiative decay back to the lowest energy state of the first excited state, (c) is the radiative decay where a photon is emitted, (d) is a triplet state excursion and its subsequent radiative relaxation back to the ground state. The numbers at the side denote the approximate time scale for the corresponding event.

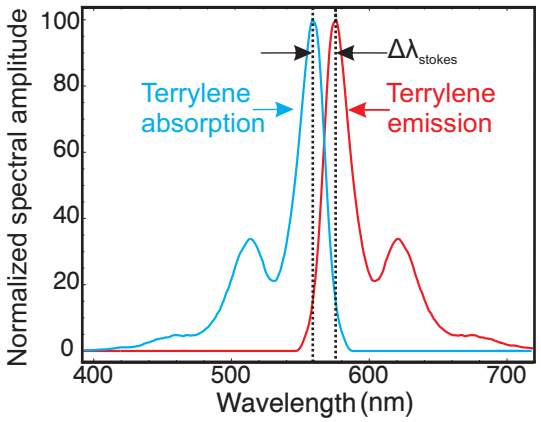

Figure 2: Absorption and emission spectrum showing Stokes shift as the difference between the absorption and emission spectra, $\Delta\lambda_{\mathrm{stokes}}$. The peak absorption of Terrylene is at 561nm and peak emission is at 575nm. This corresponds to a stokes shift of 14nm [20].

shift is dependent on temperature; higher temperatures give rise to a greater Stokes shift as electrons have more energy to be promoted to higher vibrational states, and relaxation can occur to more vibrational states of the ground state as well; increased temperature gives the molecule more vibrational energy and this is reflected in the increase in vibrational levels in $|S_0\rangle$.

The singlet state is a collection of orbitals where each orbital holds two electrons. Each electron has opposing spin from the other electron in the orbital, pursuant to the Pauli's exclusion principle. The triplet state is a state where electrons can have spins that are in the same direction in a way that does not violate the exclusion principle as the triplet state is actually consisting of three closely energy separated spin states; hence the term "triplet" state. Apart from these fundamental electronic states, addition energy levels can also be present due to vibrational motion of the molecule. These additional states are usually represented by lines above the singlet or triplet electronic states on the Jabłonski energy diagram as shown by the fine lines in Figure 1. The lines further in between each pair of vibrational states are rotational states, which are present due to rotational motions of the molecule.

Usually, molecular excitation and relaxation occurs between the HOMO and LUMO singlet states only [17]. However, there exist a non-zero probability of an interstate excursion (sometimes also referred to as an "intersystem crossing" in literature [14, 11]); where electrons transit into the triplet state from a singlet excited state; but these occurrences are rare. The converse, where the electron returns to $|S_0\rangle$ form $|T_1\rangle$ is also rare, thus the triplet state lifetime is long compared to that of the singlet states.

Therefore, when the electron is within the triplet state, the molecule **appears** dark and non-emitting. For this reason, the triplet state is sometimes referred to as the "dark state" [15, 16]. The excited lifetime in these triplet states are usually much longer than lifetimes in the excited singlet states; the triplet state has an average lifetime of 18 $\pm$ 2 μs [16]. As seen in Figure 1, the triplet state $|T_1\rangle$ has lower energy than the singlet excited state $|S_1\rangle$. Thus, electron relaxation from $|T_1\rangle$ tend to radiate low energy photons, often outside the optical range. This is the mechanism behind phosphorescence and explains its delayed, red shifted emissions with respect to the incident light. Whereas the fluorescence emission has lifetime indicated in 1c). Emission will resume again once the electron is relaxed back into the singlet ground state and the entire excitation process restarts itself upon excitation. One of the characteristic behavior of single molecules is therefore these apparent blinking effects when the electron is in the triplet state. Based on the triplet state model, other mechanisms have been forwarded to explain the observation of blinking [21, 22]. The selected host matrix in which the molecule resides in also has an influence on the photostability of the molecule. blinking effects have been observed to be far worse (that is to say, more blinking) in disordered matrices such as Poly(methyl methacrylate/methacrylic acid)(hereafter PMMA/MA) than in crystalline matrices such as *p*-terphenyl [16]. Another property that makes crystalline host matrices more favorable for use is the spectral stability of molecular fluorescence in crystalline matrices is better compared to the spectra stability of the same molecule embedded in disordered matrices [16].

Another characteristic behavior is that single molecules tend to photobleach after prolonged exposure; that is, they stop fluorescing permanently. However, unlike bulk fluorophores, when single molecules photobleach, they turn off instantly, also known as a single step bleaching event. A rigorous mechanism to explain this phenomenon has not been forthcoming, but possible explanations such as further excitation from the triplet state [14] has been forwarded in an attempt to explain photobleaching. When any of these two events have been observed to happen, one can **reasonably** conclude that one has observed a single molecule. However, care should be noted that this is not a rigorous conclusion, as several molecules can be packed together and switch off consecutively or simultaneously, thus giving the illusion of being a single molecule, although many works found in literature employ this observation as an indication that single molecules have been observed [16, 13, 12]. Measurement of the second-order correlation function is a better way of concluding an observation's single molecule status; the second-order correlation function will be described in more detail below in section 2.1.2.

The particular quantum emitter selected for the experiment is terrylene embedded in *p*-terphenyl crystalline host matrix, where the host matrix has the function of holding the molecules in place. Terrylene is used as it is known fluorescent molecule with high photostability and quantum yield [23].

In Figure 3, the red arrow shows the transition dipole moment of terrylene. From literature, it is known that *p*-terphenyl causes the transition dipole moment of terrylene to have a defined orientation pointing away from the coverslip surface[24]; this is be-

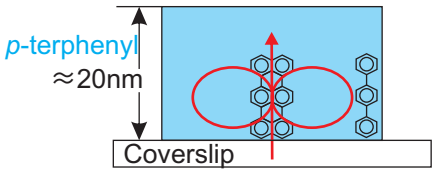

Figure 3: Transition dipole moment of a Terrylene molecule indicated by the red arrow drawn through the molecular structure of Terrylene. The red ovals beside denote the emission profile of the molecule, which resembles that of the diploe antenna. Blue colour box represents the *p*-terphenyl crystalline host matrix; molecular structure shown on the right. The molecule drawn in the middle is the Terrylene molecule whereas the molecule on the right is the molecular structure of the *p*-terphenyl host matrix molecule. Thickness of film is approximately 20nm or 20 molecular layers thick [24]. Molecules are not drawn to scale.

cause the crystalline structure causes the transition dipole moment to align itself with one of its crystal axis. The orientation of the transition dipole moment is important in determining how efficiently the molecule is absorbing the incoming light; the most efficient light absorption occurs when the polarization of the incident light is parallel to the transition dipole moment orientation. In the strong focusing regime the molecule will most likely find itself in when single molecule experiments are conducted, the excitation focus will have longitudinal polarizations which can efficiently excite the molecule, even if the incoming light has polarization transverse to the direction of propagation [17].

The circles around the molecule denotes its emission profile, it can be see that much of the light emitted by terrylene is perpenticular to the dipole moment orientation.

2.1.2 Photon bunching and anti-bunching

Photons that are spatially separated are known as anti-bunched photons. Since a single molecule can only emit a single photon at one time, due to the excitation / relaxation cycle, the photons emitted from a single molecule must be anti-bunched. The converse is also true, that detecting anti-bunched photons will also indicate that there is a single molecule under the observation. The way to measure anti-bunched light is through the use of a Hanbury Brown and Twiss setup [25] as shown in Figure 4.

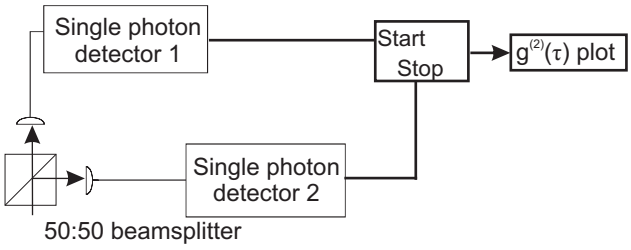

Figure 4: Schematic diagram of a Hanbury Brown and Twiss setup used to detect the second order correlation between the two detectors.

Using a 50:50 beam-splitter, incident photons can be detected by either detector 1 or 2 with equal probability. The start/stop measuring device is basically a computer which will log arrival times of the photons, with the help of a timestamp card; an external device with high temporal resolution that is able to convert photon arrival times into

computer-readable data. Due to the corpuscular nature of photons, they can never arrive at two places at one time. Thus, anti-bunched photons cannot be detected by both detectors simultaneously. The computer then calculates the time difference between each detected photon on detector 1 and every other detected photon on detector 2. Following which the information is plotted as a histogram of time differences and the total number of photons with that time difference. The normalized version of this data is the second order correlation function and is mathematically expressed as [26]:

$$g^{(2)}(\tau) = \frac{\langle I(t)I(t+\tau)\rangle}{\langle I(t)\rangle^2} \tag{1}$$

Where t is time and τ denotes the time delay between consecutive photons between the two detectors. Thus the expression in equation 1 expresses the temporal correlation of detection events between two arms; given a detection event in detector 1, what is the probability for the next detection in detector two to occur given a time difference τ.

Theoretically, if $g^{(2)}(\tau) \geq 1$, it is said that the incident light exhibits photon bunching. This is consistent with the classical theory of light and can be predicted by electromagnetic wave theory [8]. In classical theory, light can be continuously divided in irradiance into halves and activating both detectors simultaneously. However, by applying quantum mechanics to model the second order correlation function, the results yield [26, 8],

$$g^{(2)}(0) = \begin{cases} 1 - \frac{1}{n} & \forall \quad n \geq 1 \\ 0 & \forall \quad n = 0 \end{cases} \tag{2}$$

where

$$n \in \mathbb{N}$$

Where n is the same quantity as n in the number state of light, denoted as $|n\rangle$ [8, 26] in Dirac notation. The number state of light represents how many photon exists in any one particular space and time coordinate; thus the number of photons are in that particular state of light. This is analogous to intensity in the classical expression of second order correlation function, where the irradiance is proportional to the number of photons incident on a surface or detector. In the case of single molecule fluorescence, the number state of light can be attributed to the number of molecules in the focus; as at any one time, one molecule can only contribute to one photon. Thus with n number of molecules, the number of photons, is potentially n. As there are more molecules emitting photons, the normalized correlation approaches 1 and the light starts to behave in a classical manner. To demonstrate anti-bunching behavior, which correspond to a number state $|1\rangle$, equation 2 must evaluate to to less than 0.5; $g^{(2)}(\tau) \geq 0.5$ would indicate a possibility of there being more than one photon and anti-bunching is not rigorously confirmed, even if a dip is visible. Although $|0\rangle$ can also evaluate to zero at τ=0, it would also be 0 even when $\tau \neq$0. Thus it is easy to distinguish between anti-bunched light and having no light at all. Photon anti-bunching is a completely quantum mechanical phenomena and cannot be explained or predicted by classical theories of

light [8]; its manifestation involves the explanation of light in terms of corpuscular photons, which will not be in two places at once; thus yielding $g^{(2)}(0) = 0$.

Another, more intuitive way of looking at this is that if there were two molecules emitting, as one molecule emits, there is a 50% chance that the other will also emit at the same time. Thus, after measuring a large number of photons, this statistic will be manifested as a situation where $g^{(2)}(0) = 0.5$. The same argument can be extended to n number of molecules.

The need for two detectors to resolve the anti-bunching in such an indirect manner is due to the inherent dead time of the APDs [3]. Time is needed to charge up the APD depletion region after it is depleted by an electron avalanche following a photon incidence. During which, any incoming photons will not be detected or correlated, thereby giving $g^{(2)}(0) = 0$ unconditionally. If an ideal detector with no dead time is available, then there is no need for a Hanbury Brown and Twiss detection scheme [3].

2.1.3 Rate equations and analytical solutions

The dynamics of a system shown in Figure 1 can be described by a series of rate equations, which are reduced from the optical Bloch equations [11, 27]. A figure illustrating the derivations is shown in Figure 5. Note that in this analytical solutions, unlike a similar Jabłonski energy diagram in Figure 1, no vibrational or rotational states are taken into account.

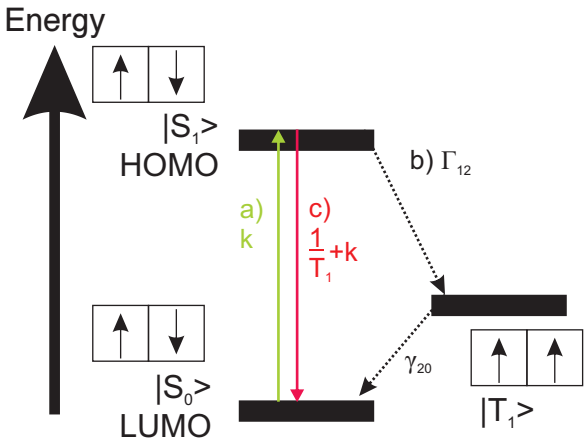

Figure 5: Energy diagram and corresponding symbols used in analytical derivation of the second order correlation function and rate equations.

The rate equations describing the dynamics of electron population in each state are [11]:

$$\frac{d\rho_0}{dt} = (\frac{1}{T_1} + k) - k\rho_0 + k\gamma_{20}\rho_2 \tag{3}$$

$$\frac{d\rho_1}{dt} = -(\Gamma + k)\rho_0 + k\rho_0 \tag{4}$$

$$\frac{d\rho_2}{dt} = \Gamma_{12}\rho_1 - \gamma_{20}\rho_2 \tag{5}$$

Where

$$\Gamma = \frac{1}{T_1} + \Gamma_{12} \tag{6}$$

Where Γ_{12} is the rate of intersystem crossing into the triplet state per second, *k* is the rate of absorption, and γ_{20} is the decay rate from the triplet state back to the single ground state, T_1 is the life time of the electron in the excited state (not to be confused with the triplet state, $|T_1\rangle$), ρ_0 & ρ_1 are the electron populations of $|S_0\rangle$ and $|S_1\rangle$ respectively and ρ_2 is the population of the triplet state, $|T_1\rangle$. Knowing the dynamics of the system will enable the derivation of the emission rates of the molecule and to construct an analytical version of the second order correlation function, $g^{(2)}(\tau)$.

Where the second order correlation function derived with this analytical method is [11],

$$\mathcal{C}(\tau) = \frac{k}{T_1}[\frac{\gamma_{20}}{\gamma_0^2 - R^2} + (1 - \frac{\gamma_{20}}{\gamma_0 - R})\frac{e^{-(\gamma_0 - R)\tau}}{2R} - (1 - \frac{\gamma_{20}}{\gamma_0 + r})\frac{e^{-(\gamma_0 + R)\tau}}{2R}] \tag{7}$$

Where

$$\gamma_0 = \frac{\Gamma + 2k + \gamma_{20}}{2} \qquad \text{and} \qquad R = \sqrt{(\frac{\Gamma + 2k - \gamma_{20}}{2})^2 - \Gamma_{12}k} \tag{8}$$

The normalized second order correlation function would then be [11],

$$g^{(2)}(\tau) = \frac{\mathcal{C}(\tau)}{\mathcal{C}(\infty)} \tag{9}$$

normalizing to the number of coincidences for infinite separation time between the arrival time of both arms. But for the purposes for the experiment, this is usually in the order of tens of microseconds.

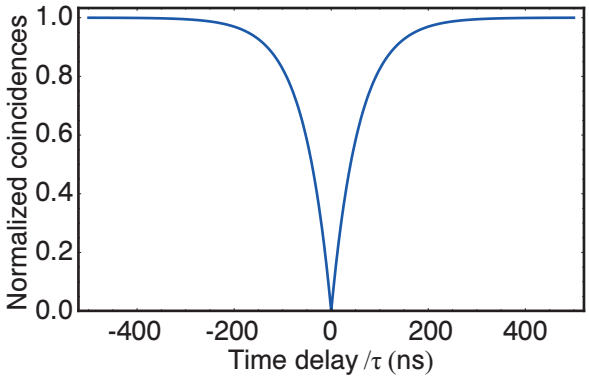

Figure 6: Idealized $g^{(2)}(\tau)$ using equation 9 and γ_{12}=6.1MHz, Γ_{12}=0.01MHz, $T_1 = \frac{1}{87MHz}$, k=0.4MHz, Γ=10MHz.

2.2 Microscopy basics

As a microscopy system is involved, basic elements of microscopy is used in handling and designing the microscope. Thus, relevant concepts are reviewed here that will be common in the day to day use of the confocal microscope.

2.2.1 Magnification

The main purpose of microscopes is to be able to magnify an small object to a reasonable size for the purposes of observation. At the heart of any microscopy system is the objective lens, which is the lens closest to the object under observation. magnification can be described as the ratio of the image size and the object size.

A value for the objective lens magnification is usually inscribed on the housing of any modern microscope objective lens, along with other vital information pertaining to the specific objective lens. An example of this is shown in Figure 7.

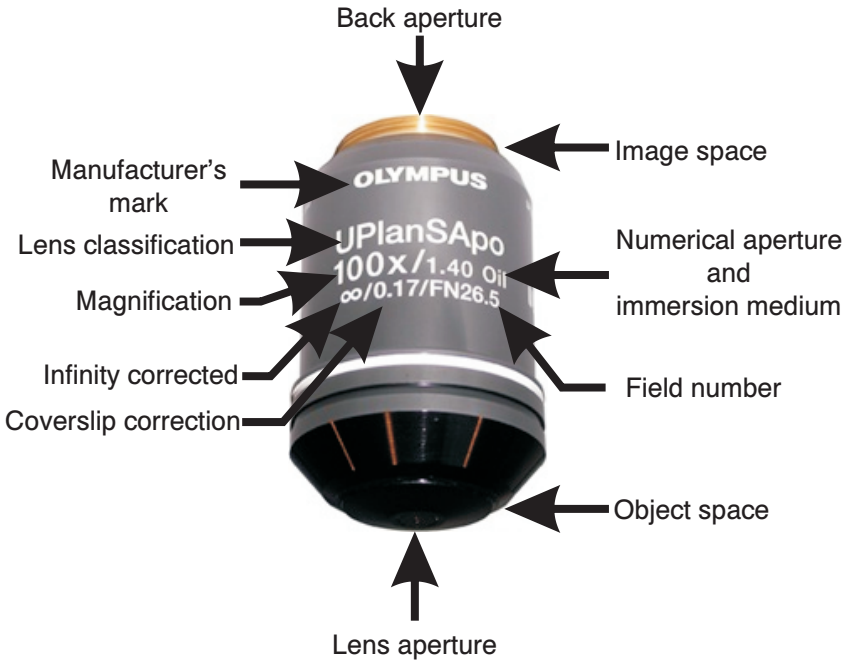

Figure 7: Example of a modern microscope objective lens. Same objective used in the project. Image of objective taken from [28];labels describing the inscription was not part of image taken from the aforementioned website.

Old objective lenses are designed so that an image converges at 160 mm away from the objective lens to form an image without the help of additional lenes, this is shown in Figure 8(a). Modern objectives are now infinity corrected, that is to say, instead of converging rays, parallel rays emerge from the lens for each point on the object and this is shown in Figure 8(b). As a result, a tube lens must be placed behind the objective lens for an image to be formed. This is shown in Figure 8(c). Infinity corrected objective lenses are marked by an ∞ sign (see Figure 7), whereas old objectives would have ”160 mm” inscribed on the housing. Notwithstanding the abolition

of the 160 mm standard, the magnification defined on the housing of the lens still adheres to that definition; i.e., the given magnification is only valid for an optical system which has a tube lens of focal length, f_{tube}=160 mm.

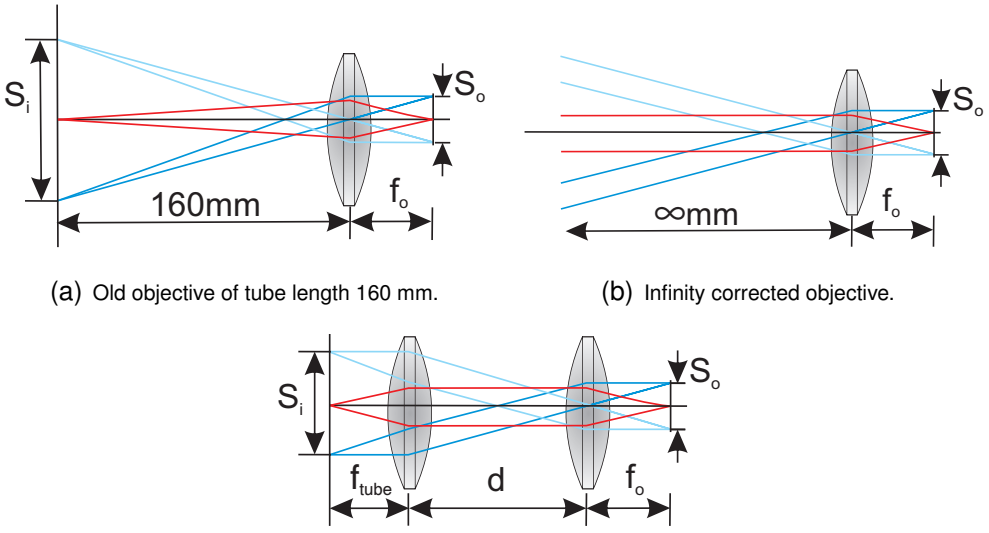

(a) Old objective of tube length 160 mm.

(b) Infinity corrected objective.

(c) Infinity corrected objective with tube lens.

Figure 8: New and old objectives, S_o denotes object size, S_i denotes image size, f_o denotes focal length of lens.

For any imaging system for which the tube lens focal length is not 160 mm, the effective magnification can be calculated by [29]:

$$M_{\text{eff}} = \frac{f_{\text{tube}}(M_{\text{obj}})}{160\ mm} = \frac{f_{tube}}{f_{obj}} = \frac{S_i}{S_o} \tag{10}$$

Where M_{eff} is the effective magnification of the system comprising of the microscope objective and the tube lens, f_{tube} is the tube lens focal length in mm, f_{tube} is the tube lens focal length in mm, M_{obj} is the magnification value given by the microscope objective housing, f_{obj} is the focal length of the microscope objective lens, S_i is the image size and S_o is the object size (see Figure 8).

2.2.2 Numerical aperture

The numerical aperture (hereafter abbreviated to NA) is a number which describes the solid angle subtended by the acceptance cone of a lens (see Figure 9 for a 2D representation of the acceptance cone). As shown below, the higher the NA, the greater the light collecting ability of the lens when observing a given spot or location.

Mathematically, the NA is defined as [6]:

$$NA = n\ sin(\alpha) \tag{11}$$

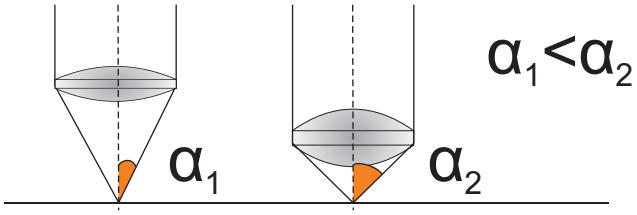

Figure 9: (Left) Lens with lower NA, (Right) Lens with higher NA. Both lenses have the same diameter, but different focal lengths. From equation 11, it can be inferred that higher NA lenses usually have shorter focal lengths than a lens with the same diameter but lower NA. Higher NA lenses tend to be thicker as well.

where n is the refractive index of the immersion medium and α is the angle highlighted in Figure 9. The physically meaning of the NA is the light gathering ability of the microscope objective lens [6]. As indicated by the word "oil" inscribed on the objective housing in Figure 7, this particular lens is an oil immersion objective lens, in which the tip of the objective facing the sample will be immersed in a microscopy oil which has a refractive index of 1.51; i.e. the value *n* in equation 11 is also 1.51.

The numerical aperture is the cardinal figure of merit for any lens and an ideal lens will have a NA value which is exactly equals to the value of n. But this would imply that α is 90 degrees. Physically, this means either the lens diameter is infinitely large, or that the focal length of the lens is zero, thus impractical in reality. It will be explained in section 2.2.3, on diffraction limitation, how the NA of a microscope objective is crucial in defining the performance of the microscope.

2.2.3 Diffraction limited focusing and resolution

The performance of an optical microscopy system is constrained by the diffraction limit. In which the effects of Fraunhofer diffraction limits the ability of a system to focus light to a spot, or to resolve distances smaller than the diffraction limit.

Diffraction limited focusing

When a coherent laser beam is being focused to a spot by the objective lens, the lens acts as a circular aperture and the resultant image of the focused spot is given below in Figure 10(b).

This diffraction pattern is known as an Airy disk and its cross-section normalized irradiance profile can be described by [6]:

$$\frac{I(\theta)}{I(0)} = [\frac{2\ J_1(ka\ sin\theta)}{ka\ sin\theta}]^2 \tag{12}$$

Where $J_1(\theta)$ is the first order Bessel function and θ is the angular displacement from the middle of the focusing aperture, k is the wavenumber of the light and a is the aperture radius. Plotting equation 12 will yield the following irradiance profile as shown in Figure 10(a). As seen, this is in excellent agreement with the picture in Figure 10(b), with the central maximum much brighter than the rest and the first order

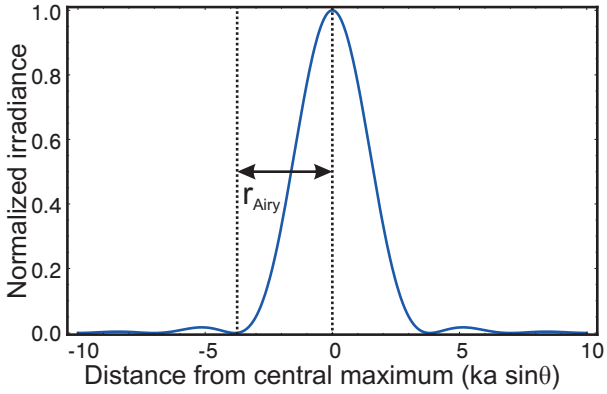

(a) Normalized Irradiance of a diffraction limited spot as a function of radial distance away from the central maximum.

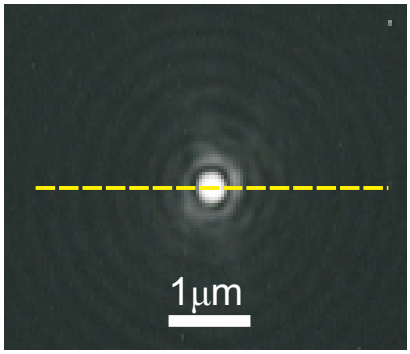

(b) An actual picture of a diffraction limited spot, yellow line a location where the cross section intensity profile is described by Figure 10(a).

Figure 10: Figures depicting the Airy disk.

ring around it only slighter brighter than the higher order rings, which are barely visible.

Where r_{Airy} indicated in Figure 10(a), the radius of the first irradiance minimum can only reach a lower-bound theoretical limit given by:

$$r_{\text{Airy}} = 0.61 \, \frac{\lambda}{\text{NA}} \tag{13}$$

Where λ is the wavelength of the light being focused.

The spot cannot be focused down any further due to the diffraction limitation and this is thus called a diffraction limited spot. As aforementioned in the closing remarks of the previous section (section 2.2.2), it is evident in equation 13 that the diffraction limited focal spot radius, which is the smallest size a laser beam can be focused down into, is highly dependent on the NA of the microscope objective. A higher NA translates to a better, smaller focus. A given radiant flux compressed into a smaller focus will yield a higher irradiance.

Diffraction limited resolution

Whereas diffraction limited focusing deals with how well light can be focused down to a spot, diffraction resolution deals with the converse situation; if given two infinitesimally small point sources, how close can they be brought together and still be resolved as two separate point sources. This distance is known as the resolution of an imaging system and a smaller value is sought after as this means smaller details can be resolved by the microscope. There are several competing yardsticks for measuring resolution [6], but we shall only consider the Rayleigh Criterion for its simplicity and practicality. The criterion states that two point sources are just resolved when the minimum of one Airy disk coincides with the maximum of the other Airy disk, as shown below in Figure 11(a).

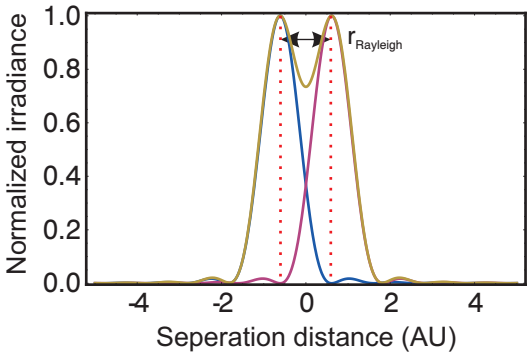

(a) Normalized irradiance spatial distribution of two diffraction limited point sources (red and blue lines). Golden line represents the addition of both sources.

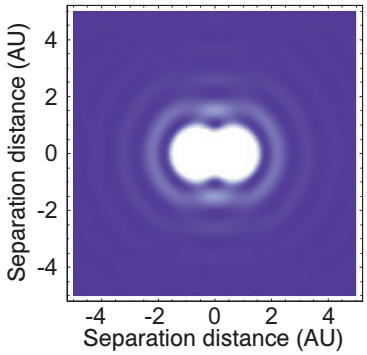

(b) Sketch of physical view of two just resolved point sources calculated using Mathematica.

Figure 11: Pictures describing two just resolved points pursuant to the Rayleigh resolution criterion.

As a result of the Rayleigh's resolution, the resolution is simply the same as the radius of the first dark ring around an Airy disk. Thus, the resolution can be calculated using equation 13; i.e. $r_{\mathrm{Airy}} = r_{\mathrm{Rayleigh}}$.

2.2.4 Microscope miscellaneous

The rest of the markings of the microscope objective housing shown in Figure 7 are explained here.

FN
The field number (hereafter referred to as the "FN") defines the field of view number of the microscope objective. This number denotes the area on the sample that can be seen; a larger FN represents the ability to see more of the sample.

Lens classification
This inscription usually indicates the type of lens in question and abbreviations used to indicate these features differs from manufacturer to manufacturer. In this case, UPLANSAPO is a combination of three qualities. U (or universal) indicates the suitability of the microscope objective for use in all illumination schemes (e.g. brightfield, darkfield, polarized light, etc). PLAN denotes that the said objective lens is capable of producing images that are uniformly focused and appear planar. SAPO is the abbreviation for superapochromatic, and it indicates that the objective lens in question has all chromatic abberations corrected to the fullest extent possible within the state of the art during the time of its manufacture.

Working distance
For most lenses, the focal length of the lens is the cardinal figure taken into account when performing analysis or calculation. It is defined as the distance from the effective focal plane of the lens to the focal point of the lens on the principal axis. The effective focal plane is the position where an ideal thin lens can reside to perform the ideal

functions of the real lens; a real lens is a lens which has a finite thickness, whereas a thin lens is an idealized lens with no thickness, but convenient for use in calculations. The working distance, however, is the distance from the tip of the microscope objective lens to the sample plane, where a collimated beam entering the lens is focused to a diffraction limited spot. It is also the position where an object resides for a focused image of the object to be form. This disparity is illustrated in Figure 12. For an immersion objective, the samples are usually placed on a coverslip facing away from the microscope objective, to prevent the sample from being contaminated by the immersion oil. The working distance for the objective depicted in Figure 7 is 0.13 mm. This objective is also used in the experiment.

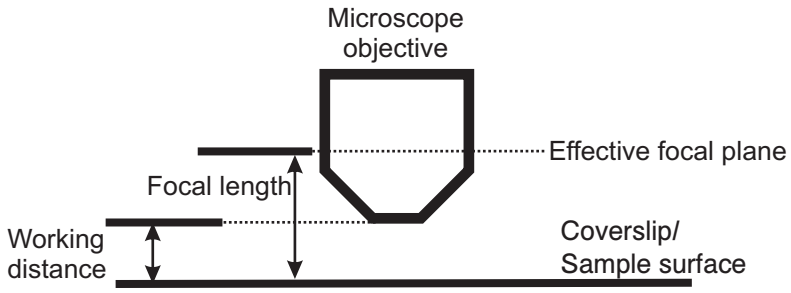

Figure 12: Working distance is the distance between the tip of the microscope objective to the sample plane or back of coverslip. This is different from the effective focal length, which is the distance between the effective focal plane of the lens and the sample plane. For an immersion objective, the working distance is the distance between the tip of the lens to the back of the coverslip, which is immersed in oil. Drawing not to scale.

Coverslip correction

The 0.17 marking on the objective lens housing denotes that this particular objective is suitable for working with a coverslip of 0.17 mm thickness. The coverslip is a thin piece of glass used to hold samples for observation under the microscope objective. Using a coverslip of thickness not matching this value can introduce a additional chromatic and spherical abberations [29]. Although for oil immersion objectives, such as this one we are using for the project, this is less of a concern as there is less refractive index mismatch between the coverslip and the immersion medium (oil) [29].

2.2.5 Widefield illumination

Widefield microscopy is the traditional optical microscopy technique that allow a user to observe a wide field of view at a time; where field of view denotes the area of the sample that can be observed. Widefield microscopy has the advantage of being easy to work with for quick observation of objects without the need for high precision or high contrast measurements.

As mentioned above, light can be send through the objective lens and focused onto a sample that is being observed. This allows the sample to be illuminated by a high irradiance as most of the radiant flux is focused and confined to a small area. However, other schemes of illumination are also possible, such as the widefield illumination. A

schematic of such an illumination technique is shown below in Figure 13.

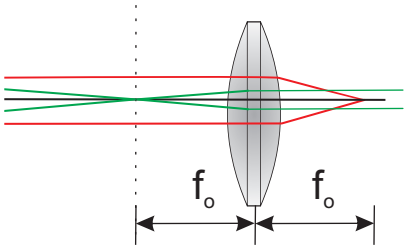

Figure 13: (Green)Wide field illumination schematically represented, (Red) Focused illumination. Dotted line indicates the back focal plane of the objective.

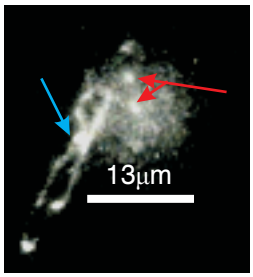

Figure 14: Picture of single molecules (indicated by red arrows) and *p*-terphenyl crystal host matrix (indicated by blue arrow) under widefield illumination.

The aim is to be able to use the objective lens to illuminate a wider area of the sample rather than just a small spot. This is done by focusing the laser onto the back focal plane of the objective lens instead of sending a collimated beam into it. The back focal plane is a plane perpendicular to the principal axis of the lens which intersects the back focal point, which is the conjugate point of the focal point of the objective lens, but located in the back aperture of the objective lens. The light coming out will be semi-directional (The collimated green beam emerging from the objective lens shown in Figure 13 is for illustration purposes only, in reality, the emerging beam is still rather divergent). Illumination area is increased at the expense of irradiance, but this is useful when high irradiance is not required but a larger illuminated area desired for quick observation.

2.2.6 Aberrations and other problems

All the analysis hitherto are done by using the first order approximation of light; in which system non-linearities are ignored. This approximation is valid if light is not forced to refract at high angles, or have too much off-axis rays (light rays which are far away from the principal axis) [6]. This is true for most applications. However, such an approximation break down when the light is forced into a strong focusing regime, as such strong focusing requires the refraction of light at extreme angles. An example of such strong focusing can be achieved by the microscope objective lens, which is able to focus a coherent light beam into a diffraction limited spot.

A breakdown of the first order approximation will introduce abberations into the images formed by the objective lens. Abberations are generally divided into monochromatic abberations and chromatic abberations. Chromatic abberations are caused by lenses having a different response to light of different wavelengths and these abberations are wavelength dependent. Monochromatic abberations are wavelength independent, as such, these abberations affect light of all wavelength equally. Although modern microscope objective lenses are able to correct most abberations, it is worthwhile to review some of the common abberations that may occur.

Spherical abberation (Monochromatic)

Spherical abberations occur when off axis light enters a lens at different incident angles as paraxial rays, (rays near to the principal axis). This is shown schematically below in Figure 15.

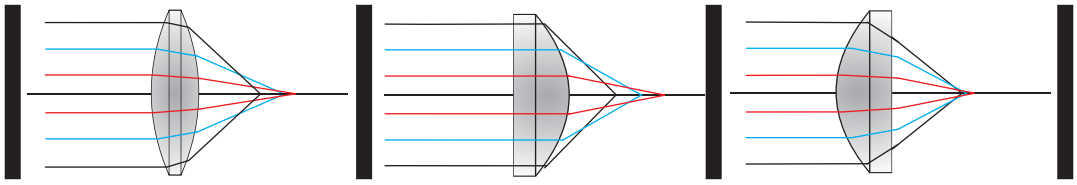

Figure 15: (Left)Spherical abberation caused by focusing of light from different parts of the lens on different longitudinal locations. (Center) and (Right) Using a plano-convex lens with the plane side facing the incoming light will increase spherical abberation. Note that the color of the ray is merely for differentiating different rays and do not denote wavelength.

Comatic abberation (Monochromatic)

The result is that images that suffer from comatic abberation will have the the off axis regions being out of focus. This is shown below in Figure 17 and schematically in Figure 16. Comatic abberation can also be caused when a lens is tilted to the object plane, causing incoming rays to focus in off-axis regions [6].

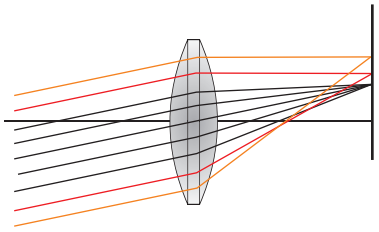

Figure 16: Object areas outside (represented by colored rays) of intended spot is now included into image being taken by the objective lens (represented by all the parallel lines, colored and black).

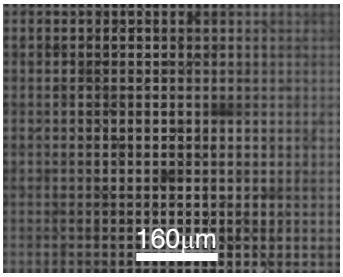

Figure 17: Outer regions of the picture is slightly out of focus due to comatic abberations. Each square corresponds to 11.5μm

Distortion abberation (Monochromatic)

Distortion abberation occurs as the magnification of a lens is a function of the off axis distance of the object. This is shown in Figures 18 and 19 below. Note that although the shape is distorted, the focus of the image is unprejudiced throughout the image. The distortion shown in Figure 19 is a form of negative distortion, also known as barrel distortion; where the sides of the image seem to bulge away from the center. The other case is known as positive, or pincushion distortion, where the sides will appear to be attracted into the middle of the image.

Chromatic abberation

As aforementioned, chromatic abberation occurs due to the lens focusing light of different wavelengths onto different points on the principal axis. This is schematically shown

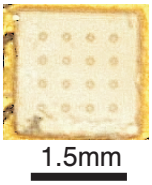

Figure 18: LED die

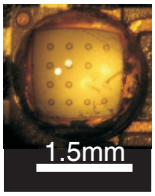

Figure 19: Same LED die as Figure 18, but with a high NA lens. Note the strong distortion abberation at the side.

below in Figure 20. However, most state of the art microscope objectives are able to correct chromatic abberations to the point where it is almost non-existent. As shown in Figure 20, light with shorter wavelength tend to focus closer to the lens compared to light with longer wavelength.

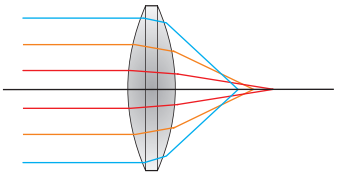

Figure 20: Different colours denote relative wavelength, with the blue ray having a shorter wavelength than the red ray.

2.3 Principles of confocal microscopy

In this section, the basics of confocal microscopy is introduced generally, focusing on the principles of operation rather than on the features of the actual confocal microscope used in the experiment, which will be covered in detail in section 3.1.

The confocal microscope was patented by Dr. Marvin Minsky in 1957. The name "confocal" is due to the fact that the detected area and illumination spot are coinciding on the same spot on the sample; i.e. confocal on the sample, that the detector see exactly what is being illuminated and nothing else [30].

Whereas conventional optical microscopy enabled the user to observe entire images at a time, confocal microscopy restricts the user to observe a small section of the object by obstructing his view via a tiny confocal pinhole. Different parts of the object is observed by moving the object on a scanning stage. Although this might sound restrictive at first, the presence of the confocal pinhole actually reduces the amount of scattering light from other parts of the sample which are not intentionally observed by the confocal pinhole [30]. As observing a tiny portion of a sample is almost of no practical utility, an irradiance tomogram is constructed by scanning the sample area of interest. The purpose of the pinhole, and the comparison to traditional microscopy is shown in Figure 21.

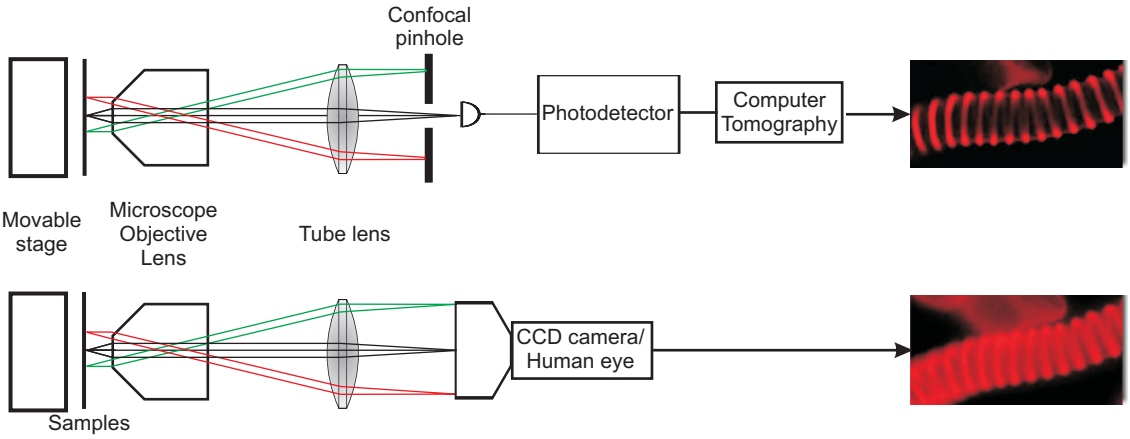

Figure 21: Comparison between confocal and traditional compound microscope. Picture taken from [31]. Note that the confocal image exhibit superior contrast and image sharpness

Wavelength discrimination to remove illumination light from fluorescence light emitted by the sample. This is shown in Figure 22. A dichroic mirror has the ability to

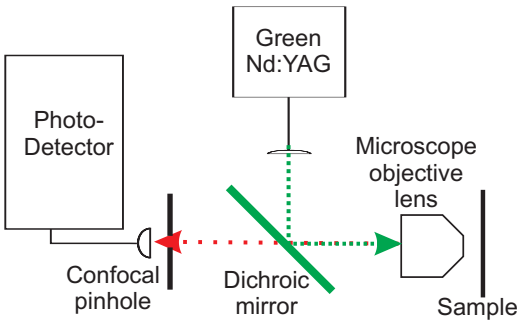

Figure 22: A bare-bone confocal microscope, to highlight the principles of operations. Note that this is different and much simpler than the confocal microscope used in the experiment.

reflect light of a certain wavelength range (in Figure 22, this corresponds to the greenish range) and transmit light that falls outside that bandwidth. Using the dichroic mirror, the laser used to illuminate the sample can lie on the back aperture side of the microscope objective lens. This allows the objective lens to be used as a focusing lens as well, taking advantage of its high NA to focus the illumination laser into a diffraction limited spot. To have light in a highly localized spot also means that areas of the sample that are not being observed are not illuminated, so stray fluorescence from other areas of the sample is less likely to occur and overexpose the area that is being observed; it will be harder to see legitimate images if the background light originating from other areas of the sample is too bright.

The illumination light reflected off the sample back into the path of the illumination laser will also be reflected again by the dichroic mirror away from the detectors and back into the illumination laser, this is true for illumination laser that underwent Rayleigh scattering at the sample surface; Rayleigh scattering is the elastic scattering of light, where the scattered light can have a different direction from the incident light, but the same wavelength as the incident light [6]. Thus, back reflected illumination light

is kept away from the detectors and this prevents the fluorescence signal from being contaminated by the illumination light. A high pass filter can be placed in front of the detector to filter off other sources of light which are not from the sample; i.e. a backup filter to remove unwanted light the dichroic mirror failed to remove.

2.4 Coherent and incoherent light

As an incoherent light source will be used in the experiment, in the form of an LED, it is useful to cover the basics of coherence theory, in particular, the difference in focusing coherent and incoherent light is discussed mathematically in the following section.

Coherence describes the correlation between the phase of two spatial points in a light field. Coherent light have a fixed phase relation between these two spatial points and as a result, light from the two spatial points can interfere and form an interference pattern. Constructive interference can cause areas of high irradiance and this is seen in the central maximum of an Airy disk as shown in Figure 10(b), which is imaged with a laser; a coherent light source. Thus, coherence is also measured by the ability of light to interfere, as will be mathematically derived below. For LEDs, a large emitting surface means that there are many individual atoms giving off light independently, thus, each mode of light given off is independent of the other modes of light given off by other atoms; they are all independently emitted and have no mutual fixed phase relation, thus they do not interfere. This concept is demonstrated schematically in Figure 23.
The quantity measuring the coherence between two spatial modes of light (denoted

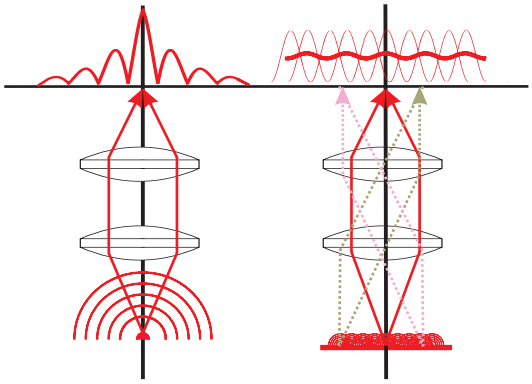

Figure 23: The difference between the focusing abilities of (Left) coherent and (Right) incoherent light. The interference on the left is supposedly an Airy disk, with side fringes exaggerated for illustrative purposes.

modes a and b) is the normalized mutual coherence function, denoted as $\tilde{\gamma}_{ab}(\tau, \vec{\mathbf{r}})$ [6], where if a=b, the quantity measures the auto-correlation of the mode. Since it is a normalized quantity,

$$0 \leq | \tilde{\gamma}_{\mathrm{ab}}(\tau_{12}, \vec{\mathbf{r}}) | \leq 1 \tag{14}$$

Where $\tilde{\gamma}_{\mathrm{ab}} \in \mathbb{C}$. For intensity on a given point ($\vec{\mathbf{r}}$) on a surface irradiated by two modes, its intensity can be given as [6],

$$I(\vec{\mathbf{r}}) = I_1(\vec{\mathbf{r}}) + I_2(\vec{\mathbf{r}}) + 2\sqrt{I_1(\vec{\mathbf{r}})\, I_2(\vec{\mathbf{r}})}\, Re[\tilde{\gamma}_{\mathrm{ab}}(\tau_{12}, \vec{\mathbf{r}})] \tag{15}$$

By using Euler's Identity, let

$$Re[\tilde{\gamma}_{\mathrm{ab}}(\tau_{12},\vec{\mathbf{r}})] = cos(\phi) \tag{16}$$

Where τ_{12} is the difference in time taken by the two modes to travel from their respective sources and is a leftover from the derivations from electromagnetic theory [6].

$$\therefore -1 \leq \ Re[\tilde{\gamma}_{\mathrm{ab}}(\tau_{12},\vec{\mathbf{r}})] \ \leq 1 \tag{17}$$

By defining a quantity to describe the contrast between the maximum and minimum irradiance magnitudes of a radiation distribution; i.e. the interference pattern's visibility,

$$\mathfrak{v} = \frac{I_{\max}(\vec{\mathbf{r}}) - I_{\min}(\vec{\mathbf{r}})}{I_{\max}(\vec{\mathbf{r}}) + I_{\min}(\vec{\mathbf{r}})} \tag{18}$$

Where due to the sinusoidal dependence of I as shown in equation 17,

$$I_{\min}(\vec{\mathbf{r}}) = I_1(\vec{\mathbf{r}}) + I_2(\vec{\mathbf{r}}) + 2\sqrt{I_1(\vec{\mathbf{r}})I_2(\vec{\mathbf{r}})} \mid \tilde{\gamma}_{\mathrm{ab}}(\tau_{12},\vec{\mathbf{r}}) \mid \tag{19}$$

$$I_{\max}(\vec{\mathbf{r}}) = I_1(\vec{\mathbf{r}}) + +I_2(\vec{\mathbf{r}}) - 2\sqrt{I_1(\vec{\mathbf{r}})I_2(\vec{\mathbf{r}})} \mid \tilde{\gamma}_{\mathrm{ab}}(\tau_{12},\vec{\mathbf{r}}) \mid \tag{20}$$

We therefore get

$$\mathfrak{v} = \frac{2\sqrt{I_1(\vec{\mathbf{r}})I_2(\vec{\mathbf{r}})} \mid \tilde{\gamma}_{\mathrm{ab}}(\tau_{12},\vec{\mathbf{r}}) \mid}{2I_1(\vec{\mathbf{r}}) + I_2(\vec{\mathbf{r}})} \tag{21}$$

If $I_1(\vec{\mathbf{r}}) = I_2(\vec{\mathbf{r}})$, as is usually the case, then

$$\mathfrak{v} = \mid \tilde{\gamma}_{\mathrm{ab}}(\tau_{12},\vec{\mathbf{r}}) \mid \tag{22}$$

That is to say, the visibility, or contrast, of the radiation pattern irradiance extrema is a direct measure of the spatial coherence of between two modes of light. The modes can be considered completely coherent when I_{min}=0, which implies that $\mid \tilde{\gamma}_{\mathrm{ab}}(\tau_{12},\vec{\mathbf{r}}) \mid$=1. Returning to Figure 23, this means that a spot of high irradiance is possible for coherent light as If $I_1(\vec{\mathbf{r}}) = I_2(\vec{\mathbf{r}})$, as is usually the case, then

$$\mid \tilde{\gamma}_{\mathrm{ab}}(\tau_{12},\vec{\mathbf{r}}) \mid = 1 \tag{23}$$

Letting $I_1(\vec{\mathbf{r}}) = I_2(\vec{\mathbf{r}}) = I_{equal}(\vec{\mathbf{r}})$, implies that for coherent light,

$$I_{max}(\vec{\mathbf{r}}) = 4I_{equal}(\vec{\mathbf{r}}) \tag{24}$$

Whereas for incoherent light,

$$I_{max}(\vec{\mathbf{r}}) = I_{min}(\vec{\mathbf{r}}) = 2I_{equal}(\vec{\mathbf{r}}) \tag{25}$$

In relation to microscopy, where focusing of light is required, this means that the focus of coherent light will always have a higher irradiance then that of incoherent light of the same radiant flux. The interference pattern is seen by focusing light to a spot is the aforementioned Airy Disk (see section on "Diffraction limited focusing" above). In figure 23, $I_1(\vec{\mathbf{r}})$ and $I_2(\vec{\mathbf{r}})$ can be view as the two dotted rays from the left and right of the right picture, which depicts incoherent light.

2.5 Colourimetry

As high power LEDs are usually used for lighting applications instead of scientific experiments, manufacturers usually prefer to express their LED optical capabilities in terms of photometric units; using Lumens (lm) or Lux (lx) as units. However, for most intents and purposes of functioning as an experimental light source, an expression in radiometric units serves a more practical function; using power or irradiance as measurement yardsticks as this corresponds directly to photon energy and is a more objective measure of optical power. Photometry and radiometry differs in that photometric measurements takes into account the human eye's spectral response when perceiving the brightness of an object. As the human eye is not equally sensitive across the entire spectrum, photometry does not provide an objective measure source exitance, especially across different coloured LEDs. The spectral response of the human eye is widely accepted to be defined by the International Commission on Illumination 1931 Resolutions on Colorimetry (hereafter CIE 1931, abbreviated from the Commission's French name, Commission Internationale de l'Eclairage). This is shown in Figure 24 [32].

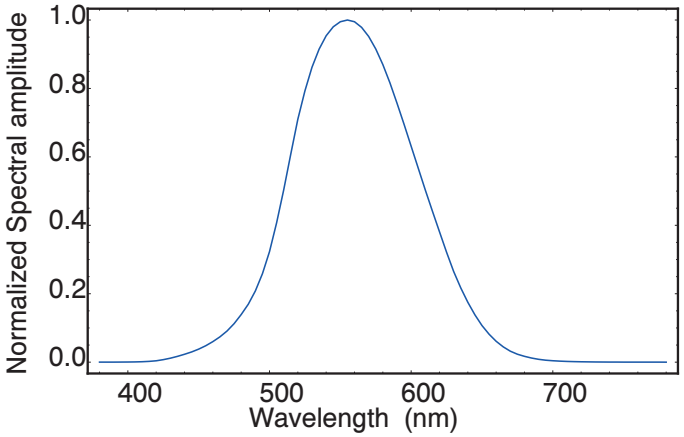

Figure 24: The normalized CIE 1931 spectral response of the human eye using photopic vision; vision adopted by the eye under well illuminated conditions.

The curve shown in Figure 24 is a normalized curve, to convert into an absolute value, simply multiply every point on the curve by the peak luminous efficacy of radiation [33], which is 683 lm/W. This value occurs at 555 nm under brightly lit conditions. That is to say the human eye is most sensitive to light with the wavelength of 555 nm under brightly lit conditions.

Letting $\mathfrak{R}(\lambda)$ denote the human eye normalized spectral response curve shown in Figure 24 and S(λ) denote the spectrum of the incident light with spectral amplitude expressed in lm/nm the conversion to a photometric spectrum, P(λ), will be

$$P(\lambda) = \mathfrak{R}(555\,nm)\ \mathfrak{R}(\lambda)\ S(\lambda) \tag{26}$$

To obtain the absolute illuminance of the incident light S(λ),

$$P = \int_{-\infty}^{\infty} \mathfrak{R}(555\,nm)\ \mathfrak{R}(\lambda)\ S(\lambda)\ d\lambda \tag{27}$$

For most experimental purposes however, it is not realistic to take infinite integration limits when only a finite bandwidth is of interest. Thus, a more realistic expression is

$$P = \int_{\lambda_1}^{\lambda_2} \mathfrak{R}(555\,nm)\ \mathfrak{R}(\lambda)\ S(\lambda)\ d\lambda \tag{28}$$

3 Practical

In this section, practical work done in the project will be reported. This discussion will mainly center around the construction and operation of the confocal microscope and description of its additional attachments such as the spectrometer and the LED light source.

3.1 Confocal microscope

A schematic diagram of the actual confocal microscope used is shown in Figure 25. The analysis of a confocal microscope system can be decomposed the detection and illumination paths. The detection path detects the light emitted by the object under observation, and the illumination path provides the light to illuminate the sample.

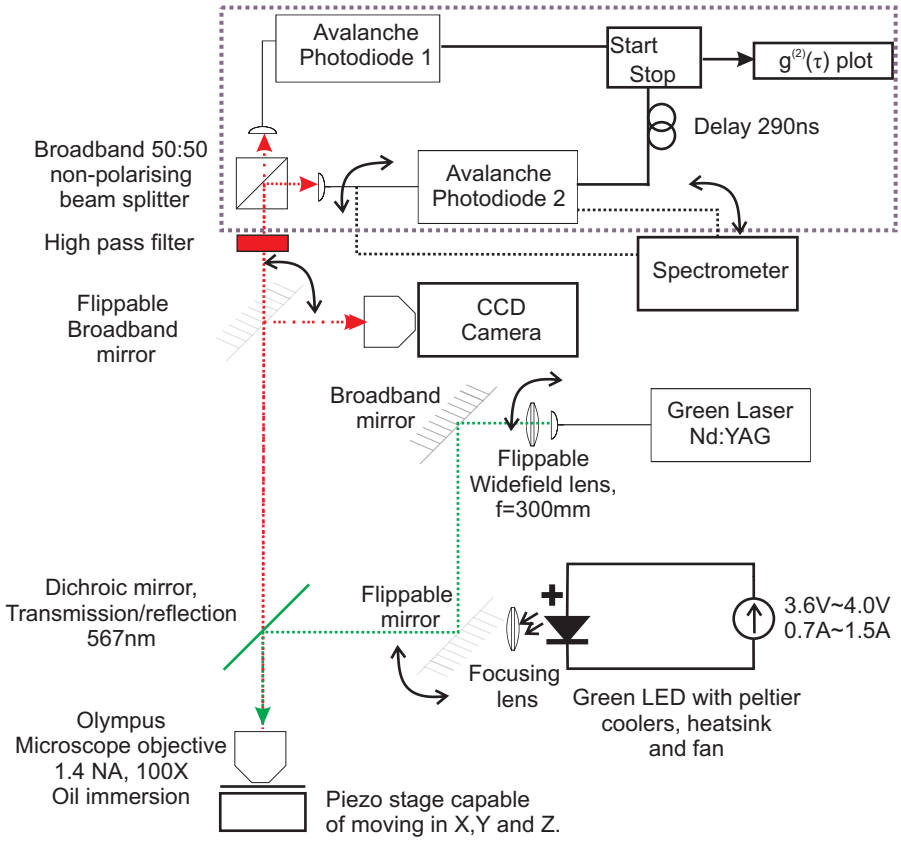

Figure 25: Schematic of confocal microscope. Hanbury Brown and Twiss setup is within the dashed box.

3.1.1 Illumination

The illumination for the confocal microscope in this experiment is provided by either an LED or a Neodymium-doped Yttrium Aluminum Garnet (Nd:YAG) laser. The Nd:YAG laser is a diode pump solid state green laser and has a maximum power of 250 μW and emits at a wavelength of 532 nm. Thus, using equation 11, the resolution of the microscope is 232 nm. The illumination laser is reflected by a series of mirror before

entering the microscope objective and focused down onto a high irradiance spot onto the sample. The alignment of the illumination beam (green dotted arrow in Figure 25) is crucial in generating quality images and good scan results. As seen in Figure 25, the illumination beam is incident on two mirrors before arriving at the dichroic. Each mirror has two degrees of freedom; adjusting the azimuth and zenith angles. Together, this allows the beam to be steered in any direction. One of these steering mirrors is before the LED illumination path and is placed on a motorized flippable mount that will allow choosing between the LED or laser illumination. A remotely controlled switch allows the mirror to flip up, reflected the laser into the microscope objective, or flip down, revealing the LED behind the mirror and allowing LED light to transmit.

The dichroic mirror used in this experiment is the Thorlabs DMLP567, with the transmission/reflection limit at 567 nm; i.e. that ideally, when light is incident 45° to the surface of the dichroic mirror, it reflects light with wavelength below 567 nm and transmits light above 567 nm. This is the key to using the wavelength discrimination technique to separate illumination and fluorescence light, as the fluorescence light has a lower wavelength than the incident light.

The goal of aligning the illumination beam is to make sure that the beam enters the microscope objective in the center and straight through. What is not shown in Figure 25 is that the microscope objective is actually facing up and there is a 45° inclined mirror looking into the objective as shown in Figure 26. This is left out for sake of brevity and ease of representation in a 2D schematic.

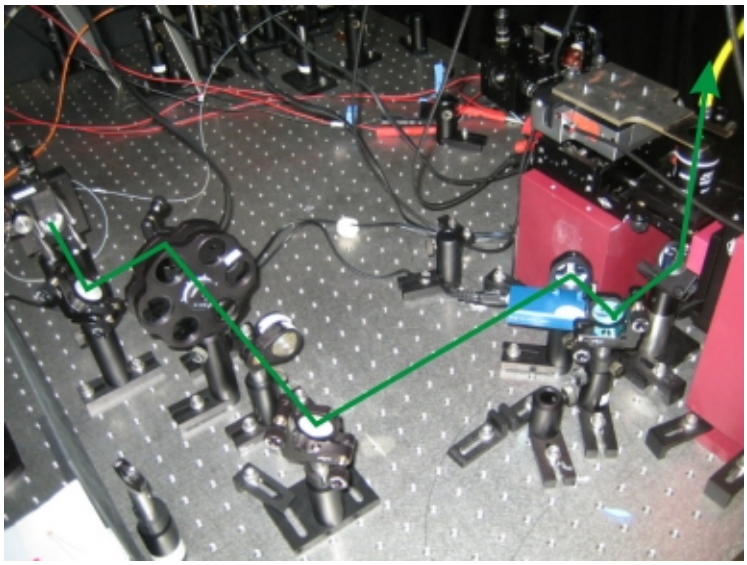

Figure 26: Partial picture of confocal microscope. Note, to the right of the picture, that objective lens is facing up and has a fold mirror at its base. Green arrow denotes illumination path taken by the excitation laser. First two steering mirrors on the left (one partially obscured) are legacy components and can be taken out without prejudice to operations. Round object on the left with holes contain two sets of neutral density filters which allows attenuation of laser irradiance. Lens tilted side ways out of beam path is the widefield lens shown in Figure 25.

Since the beam is reflected upwards, it is helpful to know the approximate path of the reflected beam, traveling normal to the ground. This can be ascertained by em-

ploying the assistance of a plumbline. As shown in Figures 27(a) and 27.

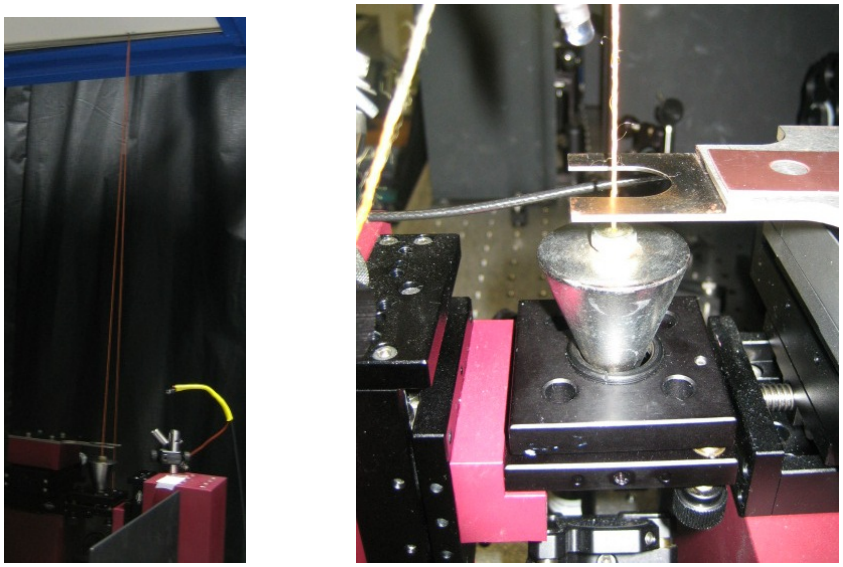

(a) Using a plumbline to trace out laser path if it were truly normal to the ground and correctly reflected by the mirror.

(b) Closeup of Figure 27(a).

Figure 27: Using a plumbline to align microscope.

In Figure 27, the hole which the plumbline cone is enter is where the objective will be screwed into. The platform which the hole is on has three adjustable knobs which allows adjustment of the tilt of the objective lens with respect to the ground. It is also crucial to make this platform perpendicular to the incoming illumination beam by adjusting these knobs. A mirror can be placed where the hole is to reflect the incoming illumination beam. If the mirror surface, hence the platform, is perpendicular to the incoming beam the reflected illumination beam will travel back at exactly along the same path and become coaxial with the incoming illumination beam. The knobs on the platform should be adjusted until this condition is observed, this will ensure that when the objective lens is screwed into the hole, the incoming illumination beam will be coaxial with the principal axis of the lens.

As seen in Figure 27(a), a spot is marked on the spot above the microscope objective position, represented by where the plumbline string touches the top structure to be marked. Every time an alignment is carried out, the illumination beam is moved to hit that spot and the center of the hole where the microscope objective is supposed to sit to ensure the beam will enter the objective lens though the center.

Unfortunately, even with all the aforementioned procedures, it still does not guarantee that the beam is absolutely entering the objective along the principal axis, but it does give a very good rough alignment and a place to start. To ensure that the beam is really coaxial to the principal axis, one must make use of the microscope objective

itself and observe the focused spot on a coverslip under magnification using the CCD camera. Ideally, an objective lens pointed perpendicularly onto a sample surface a symmetrical Airy disk should be observed. If the lens is tilted relative to the incoming beam (or *vice versa*), comatic abberations will be apparent, in the form of the Airy disk having an asymmetrical comet like profile (hence the name **comatic** abberations) instead of a symmetrically round disk [6]. This would indicate that the beam is entering the objective lens at a slightly tilted angle with respect to the principal axis. The comatic abberation can be minimized by carefully adjusting the folding mirror and the corresponding degree of freedom on the dichroic mirror to compensate for this until a symmetrical Airy disk is formed on screen. This final adjustment to correct for the comatic abberation will ensure that the beam, microscope objective lens and sample are all aligned correctly to the principal axis.

In this microscope, the objective lens will play two roles; firstly, to use its large numerical aperture to focus light down to a small spot to enhance illumination irradiance, secondly, to use that same numerical aperture to act as a collection optic to enhance the collection of single photons emitted by the fluorescence of the molecule. Detection and related issues will be discussed in the next section on detection.

3.1.2 Detection and the Hanbury Brown and Twiss setup

The role of the confocal pinhole in this setup is played by the narrow aperture of a single mode fibre at the detector, roughly 8μm in diameter. Starting from the top of the schematic, the we see that a 290 ns delay is added one detection arm of the Hanbury Brown and Twiss setup. This is due to the 128 ns dead time of the timestamp card that forms part of the start-stop measurement device, which makes it unable to measure anything after a detection even has occurred on either the "start" or "stop" input. This represents a problem in that $g^{(2)}(0) = 0$ will always occur due to the dead time, regardless of having anti-bunched photons incident on the detector or otherwise.
To compensate for this, a delay has to be added in one arm of the start stop measurement. A delay cable of approximately 58 m is added to introduce a delay in one of the arms of the start-stop measurement. This effectively shifts the τ=0 point by 290ns and now, both positive and negative time delays can be measured properly. A coaxial cable from AM Australia is used (MIL-C-17D) with a polyethylene insulator. From the manufacturer's datasheet, the phase velocity in the cable is v_{p}=2$\times$10^{8}m/s and this corresponds to the velocity expected with the measured delay time and cable length, i.e,

$$v_{\mathrm{p}} = \frac{l}{\tau_{\mathrm{delay}}} \tag{29}$$

Where τ_{delay} is the delay time between the two detector arms, which is directly due to the cable, and l is the length of the cable used. Positive time delay, $\tau >$=0, occurs when a photon activates the start arm before the stop arm and negative time delay, $\tau <$0 occurs when the stop arm actives before the start. The selection and naming of the arms are arbitrary. A actual raw data plot of the $g^{(2)}(\tau)$ is shown in Figure 28. This is before the plot is normalized to 1 and zero-shifted to yield a final plot shown in

Figure 47. The resulting $g^{(2)}(\tau)$ plot is a histogram of number of photon counts that are temporally separated by τns.

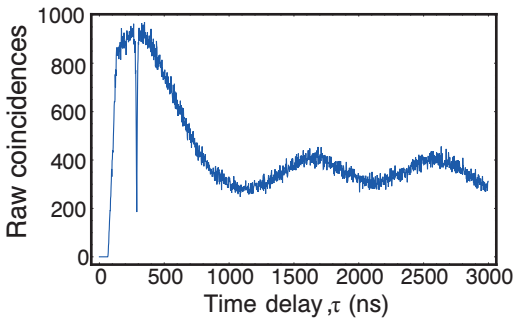

Figure 28: A raw plot of the $g^{(2)}(\tau)$ function. Note the actual anti-bunching dip at τ=290ns.

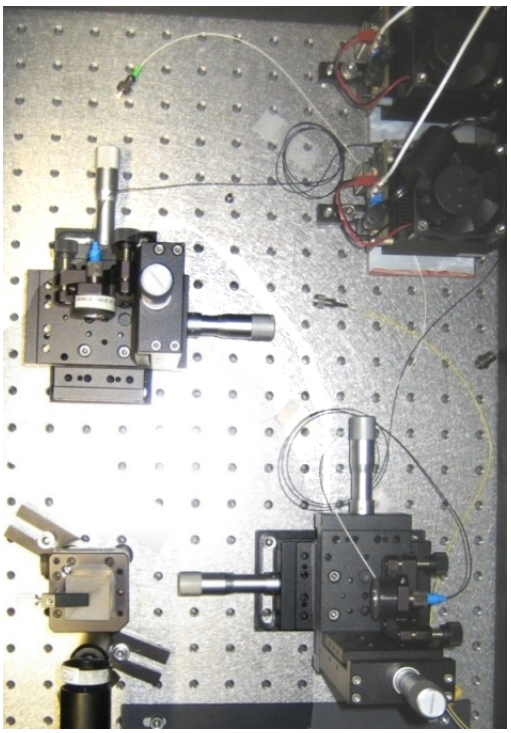

Figure 29: Actual picture of the Hanbury Brown and Twiss setup. The two black boxes at the top right hand corner are the APDs used. The square objective shown on the bottom left corner is the non-polarizing broadband beam-splitter. Just below the beam-splitter is a highpass filter. The two black objects with three silver handles hold the coupling lens, which is connected to an optical fibre from the APD.

The photo detectors used in this experiment are Avalanche photodioes (hereafter APD). The APD is pigtailed to an optical fibre, which is connected to a coupling lens, which collects and focuses light into the optical fibre. The coupling lens in turn, sits on a black mount facing the beam-splitter in the Hanbury Brown and Twiss setip as shown in Figure 29. To adjust the sensory direction of the APDs, there are four degrees of freedom to be adjusted for the coupling lens. Two to change the cartesian position of the lens, two to change the azimuth and zenith sensory orientation of the

lens. As both APDs should be taking photon statistics from the same molecule, thus, it is of cardinal import to ensure that both APDs are aligned to observe the same spot. This is done by sending a laser beam **out** of the coupling lens for both mounts, by connecting a single mode fibre between the mount and a laser. Lasers of different colours are recommended to be able to differentiate which mount needs adjustment. In the setup, a two He-Ne lasers emitting at 590 nm and 632.8 nm are used for this purpose; as both lasers have different colours and both are able to transmit through the high pass filters and dichroic mirror to reach the illumination 532 nm laser for coaxial alignment. Collimation should be the checked first to ensure all further alignments are valid. Collimation checking can be done by intuition from projecting a beam across a sufficiently large distance, or by using a shear plate collimation tester. Collimation can be adjusted by changing the coupling lens distance to the fibre ferrule.

Next, the orientation of the beam-splitter should also be checked to see if it is parallel to the ground and have surfaces normal to both input beams. This can be confirmed but turning the incline and direction of the beam-splitter so that the back reflected laser beam from each mount can be seen to light up its own optical fibre that is delivering the laser. Both beams should be combined at the beam-splitter and projected across an effectively large distance together with the illumination laser; e.g. 10m across the lab. From simple geometry, any number of cylinders can be considered coaxial if they are coaxial at two points in space. Thus, borrowing from this concept, the detector beams must be adjusted using the four degrees of freedom so that their two spots coincide in two spatial coordinates together with the illumination spot, which would have been already aligned earlier. Ideally, these two spatial coordinates selected for alignment should be as far away as possible from each other. To coincide the beams in the spot nearer to the setup, it would be more convenient to adjust the cartesian degrees of freedom and to reserve the spherical degrees of freedom for the further calibration spot. This is because spherical arc length changes due to adjusting the azimuth and zenith angles are a function of radial distances; meaning small changes in angles can result in large changes in distance in the further calibration spot while not changing the spot's position much in the nearer spot. Thus, by its very nature, the spherical degrees of freedom are more suited for calibrating the further calibration spot.

Often, it takes several iterations between trying to coincide the far and near spots to achieve coaxial beams. Additionally, the beam heights of the Hanbury Brown and Twiss setup should be coplanar with the illumination laser. Lastly, as different fibres have different ferrule lengths, it may not be advisable to change fibres connected to the mounts after the collimation has been set for that particular fibre. Instead, use a mating sleeve to connect other fibres to the calibrated fibre and avoid the need to change fibres that are already connected to the coupling lens.

Fluorescent beads are highly useful in aligning the confocal microscope and a as test sample as they approximate point sources, although with diameters of about 100nm, technically they are not point sources. They are photostable as they take very long to bleach, and they are highly fluorescent, suitable for use even in low irradiance conditions. A picture of Fluorescent beads is shown in Figure 30.

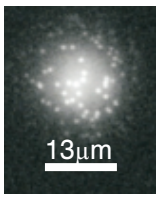

Figure 30: Picture of Fluorescent beads illuminated by a wide-field illumination of 532 nm laser.

As a final step, to ensure that both detectors are observing the exact same spot, it is advisable to adjust the azimuthal and zenith angles of the receivers by using a sparsely populated bead sample, so that both number of counts rates are the same. This would imply that both detectors are looking on the same bead.

3.1.3 Avalanche Photodiodes (APD)

The APDs have already been packaged and working in photon counting mode, having an output of NIM pulses corresponding to the detection events. More information on photon counting can be found in literature [34].

The APDs used for this experiment is the Perkin-Elmer C30902SH. From the datasheet [35], the APDs have responsivity ranging from 30 A/W at 500nm to 140 A/W at 700nm wavelength of light, which is the optical wavelengths the APDs are expected to operate at for the purposes of this experiment. The responsivity of a photodetector is the ratio of electric current flowing in the detector to the optical power incident on it [36]. The corresponding quantum efficiency ranges from 50% to 70% for the above-mentioned wavelength range. The quantum efficiency of a photodetector is the probabbilty that a single photon incident on the device will generate an electron-hole pair that contributes to the detector current [36]. The quantum efficiency is generally temperature invariant for the operational wavelength range for the purposes of this experiment. The APDs are cooled using a three stage thermoelectric cooler to a temperature of approximately -18°C to -25°C in a bid to reduce dark counts. Additional thermal conductance away from the detector is supplied by a 12V heatsink fan. The resultant dark counts are about 150 counts per second for one APD and 200 dark counts per second for the other APD. Dark counts are the number of detection events the photodiode claims it has detected even when there is no photons incident on it,thus, these values are measured simply by observing the count rate when no light is incident on the APD. The number of dark counts is temperature dependent and can be reduced by cooling the APD.

3.1.4 High pass filter

The High pass filter is an optical component that prevents light of wavelength below the cut off wavelength of the filter to transmit. The high pass filter can be placed just

before the beam splitter is used to get rid of any excitation or stray light which will contaminate the fluoresce signal and cause signal background to increase, thus decreasing the signal to background or signal to background ratio.

There is also an option to connect one of the arms of the detector to a spectrometer, where the incoming light can be decomposed to its various component wavelengths. The spectrometer also uses the avalanche photodiode(APD) as a photodetector. Thus, now the APD measures spectral amplitude of the light spectrum. For the inner workings of the spectrometer, see section 3.3.1.

3.1.5 CCD camera and magnification

The camera used is a WATEC WAT 120N-CCIR monochromatic camera with a Nikon Nikkor zoom objective lens attached (zoom objective lens on the CCD camera should not be confused with the microscope objective lens). In this case, the Nikon zoom objective is acting as the tube lens in the microscope system when the sample is viewed through the CCD camera. The zoom objective lens has an adjustable f-number, or f/#, of 4.5 to 5.4 and is used primarily to adjust the zoom and focus of the image.The f-number is a measure of a lens' light collection capability and is related to the NA. The f/# is defined as [6]

$$f/\# = \frac{f}{D} \tag{30}$$

Where f is the focal length of the lens and D is the diameter of the lens aperture. The focal length of the lens is adjustable from 80mm to 200mm, with 200mm used to focus objects at infinity. In this case, the fixture of the the zoom objective lens offers insufficient distance between the objective lens and the CCD array surface; i.e. the distance between the lens and the CCD array is smaller than the focal length of the lens, thus images are all blurred. This is solved by using additional c-mount rings which act as extenders, attached between the zoom objective lens and the camera. There is a flippable mirror in front of the CCD camera, this allows us to choose between using the CCD camera as our detection equipment or using the APDs. With the CCD camera, the setup works just like a normal microscope, allow us to see the entire sample surface at one go. Whereas using the APD is for confocal scanning, where one pixel is detected at a time. The APD is much more sensitive than the CCD camera.

Note that using equation 30, calculating for D using the two extreme values yield a different answer; i.e. D using f=80 mm and f/# = 4.5 is not equal to D calculated using f=200 mm and f/# = 5.4. This is because of an additional aperture inside the zoom objective which has a size smaller than the external lens. This limits the amount of light going in and changes the effective value of D.

In the current configuration, the focal length of the CCD zoom objective lens is set to be 200 mm to focus to objects at infinity. This will perfectly receive light that exits

the microscope objective lens as the exiting light is also corrected to focus at infinity. Using the equation 10, the current configuration has a magnification of 125X.

3.1.6 Piezo stage and controller

The piezo stage used to move a sample around is shown and this is shown in Figure 31.

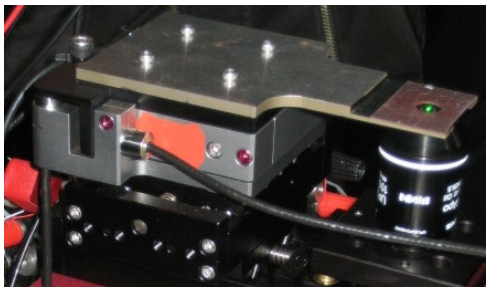

(a) piezo stage supporting a fork which holds the sample coverslip.

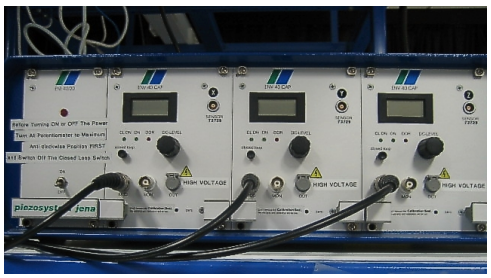

(b) Controller for piezo stage, knobs allow for manual control of piezo stage.

Figure 31: Pictures of piezo stage and its controller.

It is from Piezosystem Jena and has a translation range of 80 μm $\times$ 80 μm $\times$ 80 μm in all three cartesian axes. It is capable of operating in closed loop control mode and this enables high repeatability in locating a given position. Also, operating in closed loop mode reduces the drift that might occur when operating in open loop mode; leaving a piezo stage alone for an hour in open loop mode might cause the piezo stage to lose its intended positioning. However, the translation range is higher when operating in open loop mode; up to 100 μm $\times$ 100 μm $\times$ 100 μm. The spatial resolution of the piezo stage is 1 nm. The piezo stage is controlled by three control voltage channels from the computer that modulates between 0V to 10V, one channel for each axis. This modulation voltage is translated linearly into distance translation on the piezo stage by the controller. The controller will in turn, apply a voltage from -10V to 150V on the piezo stage to drive the stage around. The stage is predominantly used in the positive voltage regime; from 0V to 150V.

In Figure 32, a grid usually used for transmission electron microscopes is scanned in confocal mode. Each individual square on in Figure 32(a) is 11.5μm across. The result is shown in Figure 32(b).

3.1.7 Opto-mechanics

As seen from Figure 33, the confocal microscope had gone through a physical redesign. It was decided to reconfigure the microscope as this allows the use of the optical table and brings much needed flexibility in altering the topology of various components of the confocal microscope to suit the nature of the experiment; to have form follow function. Before the redesign, the setup was mounted on a vertical breadboard

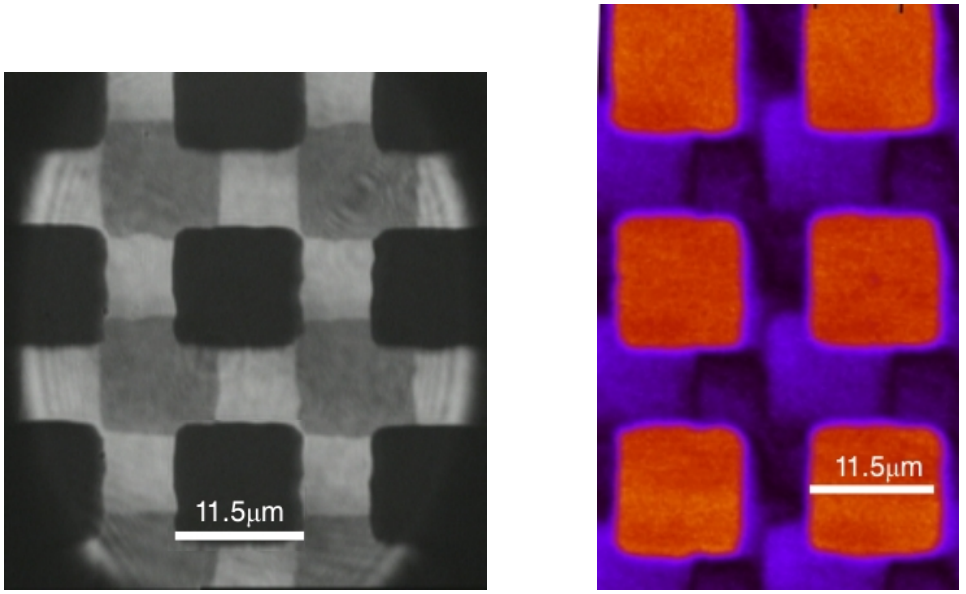

(a) Picture of grids being scanned as viewed from the CCD camera. Each square is 11.5μm across

(b) Confocal scan of calibration grids.

Figure 32: Comparison of CCD image and confocal scan.

as shown in Figure 33(a) when it was first inherited. After the re-design, it is as shown in Figure 33(b). The red blocks which were missing in the old setup is shown in Figure 34.

These blocks are created by using a computerized numerical control (hereafter CNC) machine. The programming of these machines is in a language known as G-code. The design drawings of these components are shown in the appendices.

Another advantage of this new setup is that now, the microscope objective lens is facing upwards instead of downwards. This reduces the danger of crashing the microscope objective lens into the sample when the objective lens is over driven; this can happen when the user is trying to obtain a focus, but has already gone beyond the plane of focus without knowing it. As in the old configuration, the entire weight of the objective lens will bear onto the coverslip, causing it to break as it is compressed between the old holder and the objective lens. The shattering glass may scratch the objective lens, rendering it unusable. In the new configuration, the microscope objective lens will merely push the coverslip and cause it to balance on the microscope objective lens instead. Also, changing of samples is easier with the new objective lens now that the user does not have to drive the objective up just to change a sample as the sample is easily accessible from the top, not compressed between the microscope objective and the stage below.

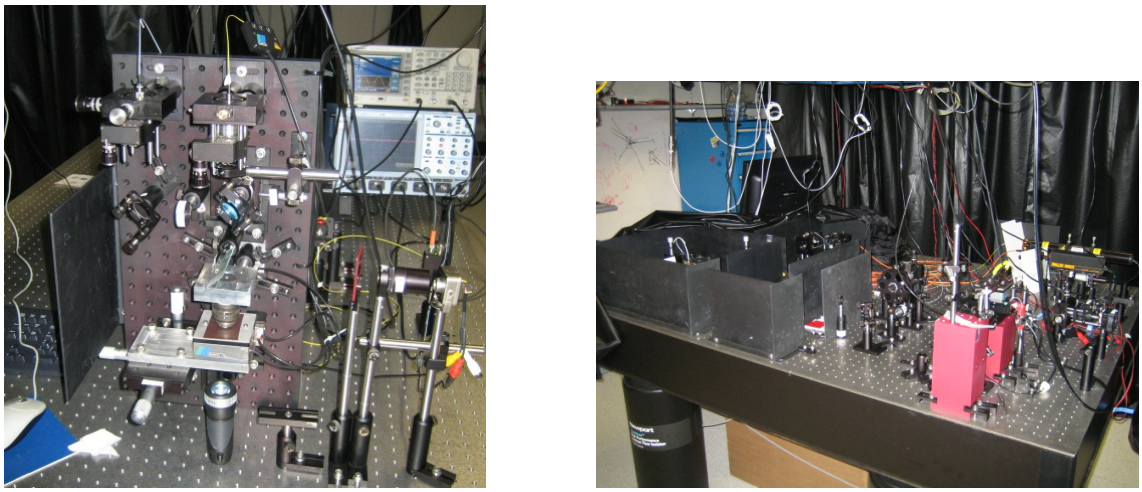

(a) Inherited setup.

(b) Setup *status quo*.

Figure 33: Setup now and then.

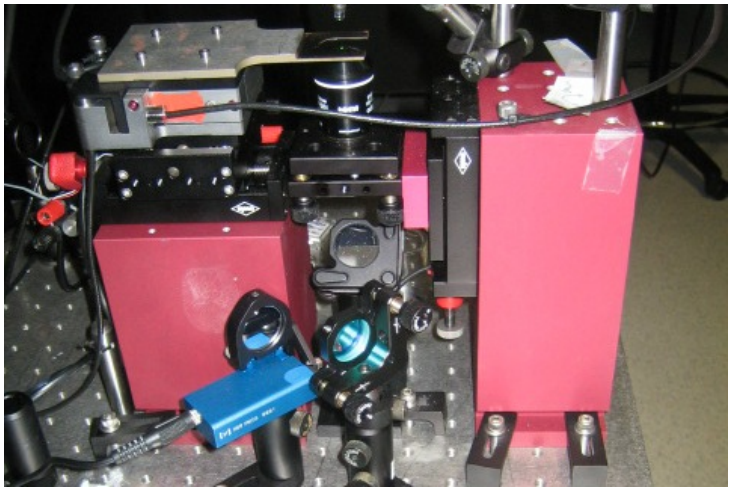

Figure 34: Red blocks and silver fork on top are new additions to the microscope design.

3.2 Light emitting diodes (LEDs)

As LEDs are extensively used in the experiment, a summary of work done on LEDs is given here. Noting the physical features, spectral and optical characteristics.

3.2.1 LED physical structure

The various subfigures of Figure 35 shows different views of a typical high power LED, in this case, selected to be the Luxeon K2 for illustration purposes notwithstanding not being used heavily in the experiment. The Luxeon Rebel, which is used in the experiment, does not have physical characteristics such as bonding wires or a large lens as in in Figure 35(b) and 35(c) respectively. In Figure 35(b), the red object in the middle is the LED die (sometimes referred to as the LED chip) and is the light emitting object of the LED. The two golden objects rising out of the sides are bonding wires and

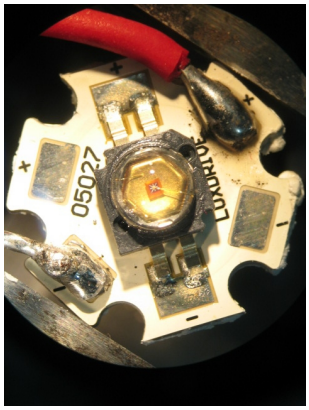

(a) A picture of the Luxeon K2 LED.

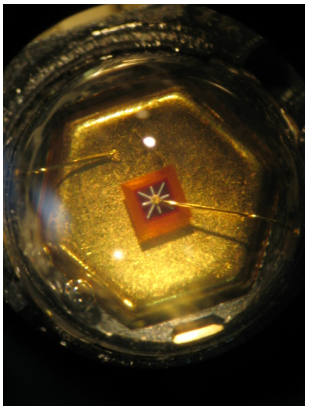

(b) A picture of the Luxeon K2 LED die.

(c) A picture of the Luxeon K2 LED side view, showing the plastic cap.

Figure 35: Pictures of Luxeon K2 LED, predominantly not used in the experiment but selected for illustration purposes due to the presence bonding wires which are not present if the Luxeon Rebel LED is used here; the Rebel is used heavily in the experiment.

are responsible for current flow to and from the LED die. In 35(c), a large lens is on top of the LED die and this is used to protect the LED die and direct the LED emission pattern.

3.2.2 LED Holder

As the high power LEDs tend to generate alot of heat, a suitable heat sink is needed. Also, a holder is required for routine experimental use, just to hold the LED in a stable, stationary position. Eventually, active cooling mechanism including a three stage thermoelectric cooler and a heatsink fan was added to bring the temperature of the LED down. This enables the LED to be driven to higher currents and have a higher optical exitance.

Holes are drilled to be able to screw the heatsink fans behind and four rods are screwed in front so that lenses can be put before the LED, as shown in Figure 36(b). The thermoelectriccoolers and LED are held in place using a piece of plastic holder sheet screwed down using four screws at the side. In Figure 36(a), a thin heat resistant plastic sheet is used when a thick piece might hinder lens placement before the LED, as shown in Figure 36(b). All holes are drilled using a CNC machine. The thermoelectriccoolers, or peltiers, have a maximum current of 4.5 A with a voltage of 8.6 V and is ran at this rating during normal operations. The heatsink fan used is a 12 V and 0.1 A DC fan. All three items are powered using power supply units located near the experimental setup.

Measurements and design of the heatsink are shown in the Appendix A.

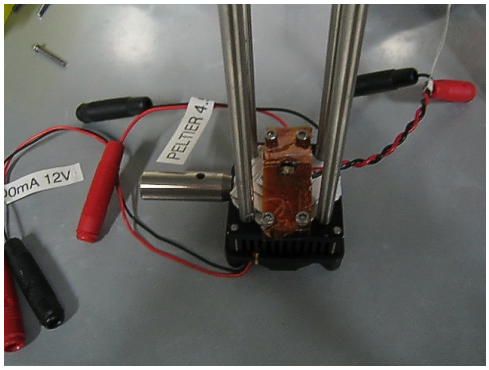

(a) LED holder. LED held against thermoelectric cooler using a yellow plastic sheet made from 3M heat resistant tape. Three electrical plugs are for LED, heatsink fan and thermoelectric cooler.

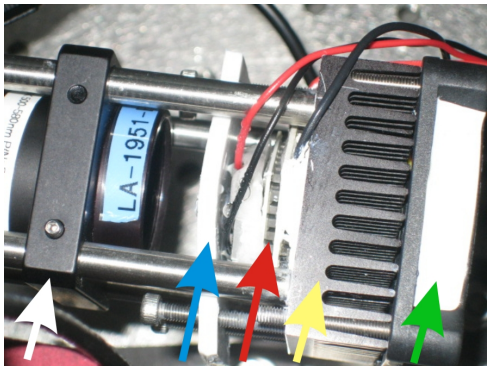

(b) (Left to right) White arrow: Lens assembly. Blue arrow: Teflon holder for pressing LED on the peltier. Red arrow: Peltier, or thermoelectric cooler, LED between peltier and teflon holder. View of LED blocked by ice formation. Yellow arrow: Heatsink. Green arrow: Heatsink fan.

Figure 36: Picture of LED holder.

3.2.3 Characterization

In this section, the range of LEDs that was auditioned for use in this experiment and the selection process will be documented.

As the Nd:YAG laser emits at 532 nm, a matching green LED was needed to replace it as a light source. The dominant brand of LEDs in the market was made by Phillips Lumileds. The following LEDs were selected as possible candidates for the eventual experiment. The first LED to be tried out is the Luxeon III star. The ease of mounting the Star shaped PCB influenced the purchase of future LEDs to have this PCB as well.

The emitted optical power (or output radiant flux) of the LEDs are measured by placing a Newport Model 840 photodiode as close as possible to the LED die, often pressed lightly against the plastic dome encasing the LED die. The photodiode has a 1 cm^2 surface. Next, there is a need to measure the exitance of the LED. Since the emitted optical power is measured with a photodiode, the exitance can be determined by knowing the die size of the LED; the exitance is the emitted optical power per unit area.

Referring to Figure 37, if y_o=f_o, f_o being the focal length of the lens, then the object focuses at infinity. If y_o=2f_o, twice the focal length of the lens, then the object focuses at 2f_o as well. Varying between the two extremes, we find a value $f_o \leq y_o \leq 2f_o$ to focus an object at an finite distance within the confines of the laboratory and with a magnification. The object is now the small LED die that is lit up and projected by the lens to a magnified image on the wall, very much analogous to a projector. That would allow the measurement of the LED die image size, S_i, accurately with a ruler.

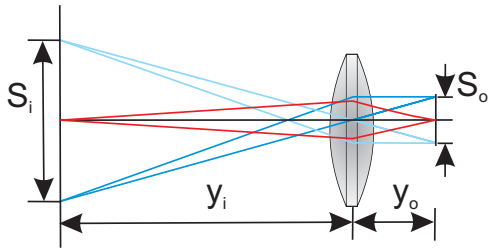

Figure 37: Imaging and magnifying LED die on a screen far away. S_o being the object size, S_i being the image size, y_o being the object distance from the lens and y_o being the image distance from the lens

Noting that transverse magnification [6],

$$M_T = \frac{y_i}{y_o} = \frac{S_i}{S_o} \tag{31}$$

With measured S_i, y_o and y_i, S_o can be easily calculated using equation 31.

LED	Maximum current (mA)	Voltage (V)	Radiant flux (mW)	Die area (mm^2)	Exitance (KW/m^2)
Luxeon III	1000	3.6	113	2.465	46
Luxeon K2	1500	4.1	147	2.465	59
Luxeon Rebel	700	3.3	198	2.465	80

Table 1: Table of different green LEDs tested. Maximum current is taken from datasheet.

The specific model numbers for the LEDs are, for the Luxeon III, LXHL-LM3C. The Luxeon K2, LXK2-PM14-U00 and for the Luxeon Rebel, LXML-PM01-0080. From Table 1, it is clear that the Rebel is the LED of choice. Moreover, looking at Figure 38, it is possible to see that the Rebel has a narrower spectrum. Thus, more of the radiant flux will be focused in the relevant spectral range in the Rebel compared to the the other LEDs. Using an *ad-hoc* yardstick to compare exitance per FWHM spectral linewidth nm, we see that the Luxeon Rebel has a most of the light concentrated within the spectral region around the dominant wavelength; this name is shown in Table 2. This will be important when a filter is used in front of the LED to filter off unwanted light too far beyond the dominant wavelength. Thus, having optical power in those spectral areas may even complicate the filtering process (see Section 4.2.1 for more on spectral filtering).

In the course of looking at the different LEDs, it is discovered that there are two varieties of Luxeon Rebel LEDs, both having the model number LXML-PM01-0080. The LED with the white die often has more optical power output compared to the LED with the black die.

By using appropriate cooling methods described in section 3.2.2, the LED will be driven over the rated limit of 700mA. The LED radiant flux vs input current curve is plotted in Figure 40. As these values are taken when the LED is cooled, the values

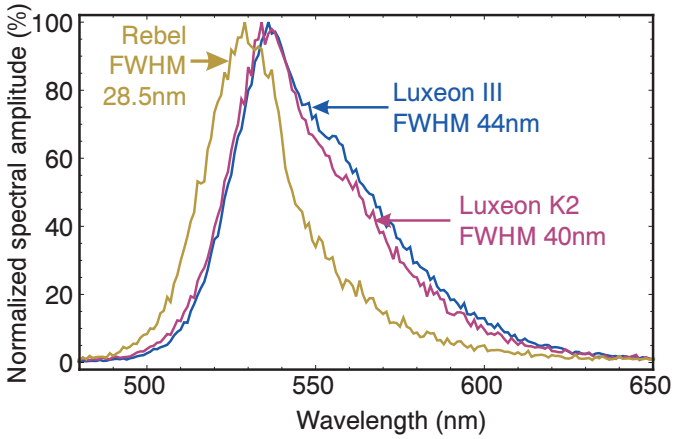

Figure 38: Spectrum of all green LEDs tried out.

LED	FWHM (nm)	Exitance per FWHM Spectral width (mW/(mm^2 nm))
Luxeon III	44	1.04
Luxeon K2	40	1.49
Luxeon Rebel	28.5	4.47

Table 2: Table of exitance per FWHM spectral width for different green LEDs tested.

differ from those given in Tables 1 and 2.

As seen from Figure 40, the conversion efficiency of the curve drops as indicated by the leveling of the curve as current increases. Thus, overdriving the LED is only effective up to a certain point and the LED is ran at 1.5A for the experiment.

Lastly, the LED has a Lambertian emission profile. That is to say, its intensity varies according to Lambert's cosine law [37]:

$$I(\theta) = \int BdScos(\theta) \tag{32}$$

Where B represents the radiance of the emitting surface, dS is an infinitesimal area on the emitting surface and θ is the angular displacement from the direction which is normal to the surface of dS. Radiance is the irradiance per unit solid angle. It can be seen that I(0)=$\int$B dS is the highest value of I(θ); that is to say, the LED's optical output, or its radiant flux, is mostly in the forward direction of the LED emission.

From equation 28, taking limits between 400 nm and 800 nm and using the measured spectrums of the Luxeon Rebel LED, the peak spectral amplitude of 7 mW can be calculated from the nominal value of 145 lm at 700 mA given in the datasheet. Converting to radiant flux, this would correspond to 270 mW at 700 mA. This agrees well with measurements presented in Figure 40 even when more complex methods in literature involving the use of integrating spheres and defined standards [38] were not

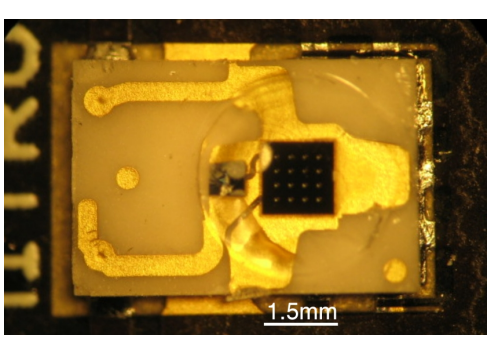

(a) A picture of the Luxeon Rebel LED with a shiny black die.

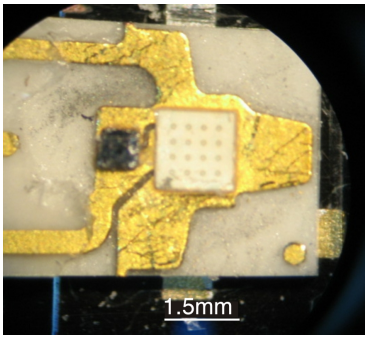

(b) A picture of the Luxeon Rebel LED with a white die.

Figure 39: Rebel die types.

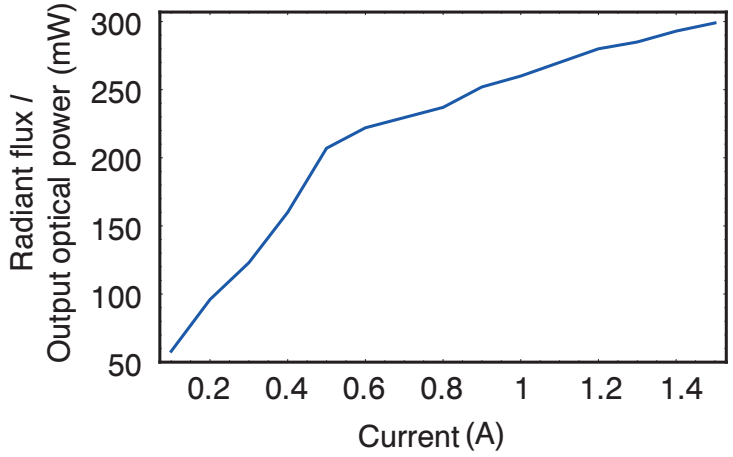

Figure 40: Green Rebel LED radiant flux vs input current.

used.

3.3 Spectrometer

3.3.1 Principles of operation

Shown in Figure 41 is a schematic of a spectrometer. At the heart of this spectrometer is a reflection grating. It is basically a piece of substrate with very fine trenches carved out on the surface of the substrate. The grating used in this experiment has a trench width of just 833nm or 1200 trenches per millimeter, denoted as "a" in Figure 41. Note that for the purposes of illustration, the trench is defined here as containing part of the top plateau as well. As shown in Figure 41, when a beam of light is incident on the surface of the grating, several orders of reflection is observed off the grating. The zeroth order being the reflection order that obeys the law of reflection where the angle of reflection is equivalent to the angle of incidence. The orders of reflection are governed by the grating equation reproduced below [6],

$$\frac{m\lambda}{a} = sin\theta_m - sin\theta_i \tag{33}$$

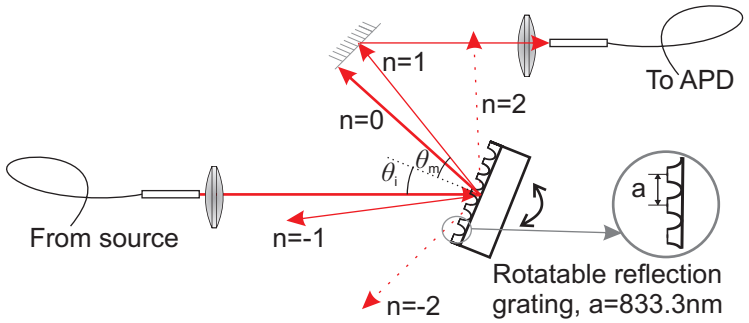

Figure 41: Schematic of a spectrometer, reflection grating is placed on a stepper motor and controlled by a motor driver. n denotes the n^{th} order reflection, with the zeroth order reflection is the same as the incidence angle, i.e. $\theta_0 = \theta_i$.

Where m is the order of reflection, a is the grating spacing between two adjacent grating peaks as illustrated in Figure 41, θ_i is the incidence angle and θ_m is the angle of reflection for the m^{th} order. These notations are illustrated in Figure 41. Thus, the angle of reflection for higher order reflections is a function of wavelength, thus a beam of light of multiple wavelengths will be broken up into a radial spectrum by the grating. As the grating turns, only one wavelength should be reflected into the detection path by the mirror. This would be especially true if a single mode fibre is placed at the end of the detection path; as it will only allow one mode and one wavelength to be measured at any one time. Therefore, using a single mode fibre will usually give a higher spectral resolution.

The spectrometer topology used in this experiment is specifically designed so that when θ_i=0, the 1^{st} order reflection of a 632.8 nm He-Ne laser is exactly being detected by the spectrometer. Having a such a laser at hand makes the alignment of the spectrometer easy as the 632.8 nm laser is able to act as a control measurement for alignment. The angular displacement between the source beam and the mirror can be calculated easily using this scenario and equation 33 by setting λ=632.8 nm, θ_i=0, m=1, a=833 nm. This means that the angular displacement between the source beam and the mirror is 49.434° or 0.8627 rad. This value is fixed as the components of the spectrometer and is a constant throughout the spectrometer operation.

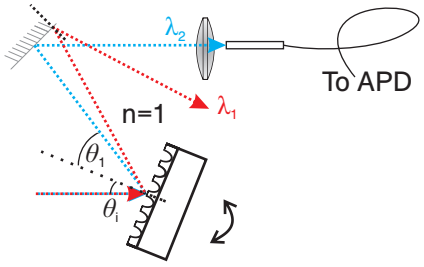

Figure 42: First order reflection is a function of wavelength. Colour is indicative of relative wavelength; $\lambda_1 > \lambda_2$.

Here, an equation to relate grating angle and the wavelength being observed by the detection arm will be derived. Since the spectrometer is supposed to work in only the first order reflection mode, therefore, m=1. As illustrated in Figure 42, the grating

angle , driven by the stepper motor, is equal to the incidence angle θ_i and will be used interchangeably hereafter. Therefore equation 33 will now be

$$\frac{\lambda}{833nm} = sin\theta_1 - sin\theta_i \tag{34}$$

As above-mentioned,

$$\theta_i + \theta_1 = 49.434^\circ \tag{35}$$

Substituting 35 into 34

$$\therefore sin(49.434^\circ - \theta_i) - sin(\theta_i) = \frac{\lambda}{833nm} \tag{36}$$

Using identity,

$$sin(\alpha \pm \beta) = sin(\alpha)cos(\beta) \pm cos(\alpha)sin(\beta) \tag{37}$$

$$0.7584cos(\theta_{\text{mot}}) - 1.651sin(\theta_{\text{mot}}) = 1.2 \times 10^6\lambda \tag{38}$$

Using identity,

$$\alpha cos(\theta) \pm \beta sin(\theta) = \sqrt{\alpha^2 + \beta^2}cos(\theta \mp \gamma) \tag{39}$$

Where $\gamma = tan^{-1}(\frac{\beta}{\alpha})$
We arrive at the equation to express wavelength being observed by detector in terms of motor angle,

$$\lambda = 1.514 \times 10^6 cos(\theta_i + 1.1404)m \tag{40}$$

Or conversely,

$$\theta_i = cos^{-1}(660.22 \times 10^3\lambda) - 1.14rad \tag{41}$$

Note that angle of grating, $\theta_i < 49.434^\circ$ to prevent the zeroth order reflection from being observed by the detector, thereby operating beyond the first order regime. This equation is currently programmed within the motor controller and rounds off automatically.

However, for convenience sake, one can also take a linear approximation. By plotting the graph for,$\frac{d\theta}{d\lambda}$, we can approximate the number of motor steps to move in order to change the observed spectral wavelength. This will be shown below. Noting that [39],

$$\frac{d\ cos^{-1}(\theta)}{d\lambda} = -\frac{1}{\sqrt{1-\theta^2}} \tag{42}$$

$$\therefore \frac{d\theta_i}{d\lambda} = -\frac{6558857.44}{\sqrt{1 - 4.30186 \times 10^{11}\lambda^2}} rad/m \tag{43}$$

Converting the rad/m expression to number of motorized steps per nm is trivial, as the stepper motor used has, mathematically, 3642.88 steps per degree.
Thus,

$$\frac{d\theta_i}{d\lambda} = -(10^{-9})(3642.88)(\frac{180}{\pi})\frac{6558857.44}{\sqrt{1 - 4.30186 \times 10^{11}\lambda^2}} steps/nm \tag{44}$$

By plotting equation (44), shown in Figure 43, we see that the number of steps per nm is roughly 150 for the operational wavelength we usually work at (400nm to 800nm). That is to say, moving by 150 steps will change from observing 600nm to

601nm or 599nm, depending on the direction turned. This is especially useful in aligning the spectrometer. Usually, the spectrometer might only be a few nm off but has the correct profile. All that would be needed is to reset the zero point where the spectrometer is calibrated at. This approximation makes it easy to find the number of steps needed to move from looking at how many nanometers the spectrum is off the desired target; during alignment, the desired target is the He-Ne 632.8nm. The zero can be reset after moving the grating to compensate for the offset inaccuracies.

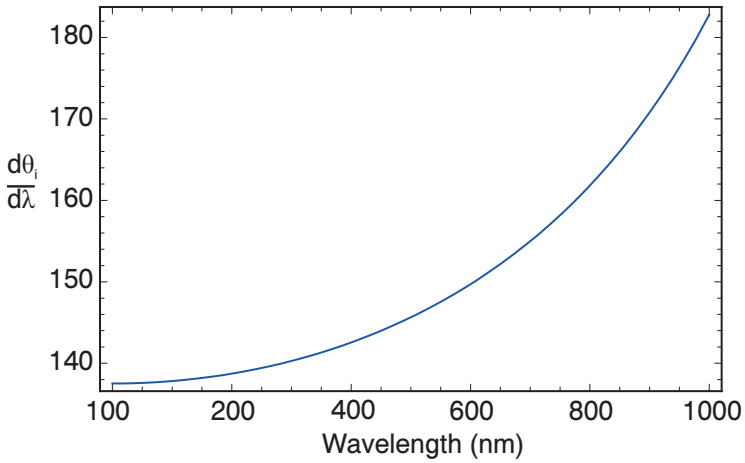

Figure 43: Number of steps to turn to move observation by 1nm.

To align the spectrometer, firstly check that the first order reflections on both sides of the grating are of the same height over a long distance, this will ensure that grating is parallel to the ground. As the He-Ne laser is likely to hit the laser when the grating is at its default position with its surface normal to the incoming beam, a lower wavelength laser beam can be used instead to facilitate the projection of the reflection over a larger distance. Secondly, the mirror is mounted in such a way that there are two degrees of freedom to be adjusted; its azimuth and zenith angles. Adjust these angles such that the reflected beam is in the same plane as the two first order reflected beams earlier. Lastly, adjust the focusing lens which will couple the light into the optical fibre connected to the APD. This lens is extremely sensitive to movement and its correct position is crucial to the alignment of the system, thus, positioning of this lens on a micrometer positioning system is advised. By reading off the APD, minor adjustments to all three angles can be made to maximize the APD reading, thereby ensuring the highest coupling efficiency into the APD.

3.3.2 Characterization

The throughput of the spectrometer is measured by plugging in 700μW of He-Ne laser light and measuring approximately 200μW of output optical power. This implies that the throughput of the spectrometer is 28%; that is, 28% of the light is in one of the first order reflections off the grating. This is to be expected the measured power is only one of the two first order reflections. Optical power is lost to the other first order reflection,

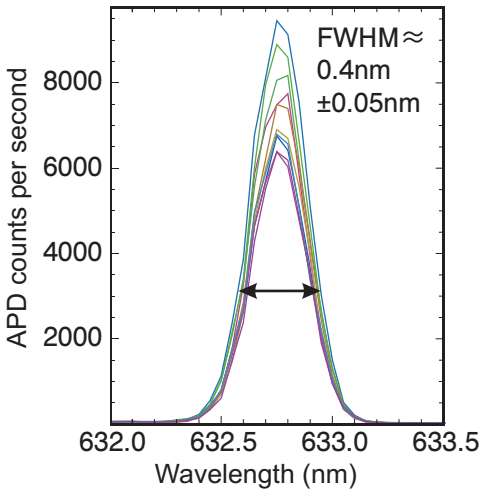

Figure 44: Results of a test measuring a He-Ne 632.8nm laser spectrum 10 consecutive times. Amplitude fluctuation can be explained by irradiance fluctuation of the He-Ne laser used, which can even be see by the unaided eye. Spectral profile consistency and accuracy are satisfactory. Arrow indicates full width half maximum (hereafter FWHM), which is about 0.4 nm.

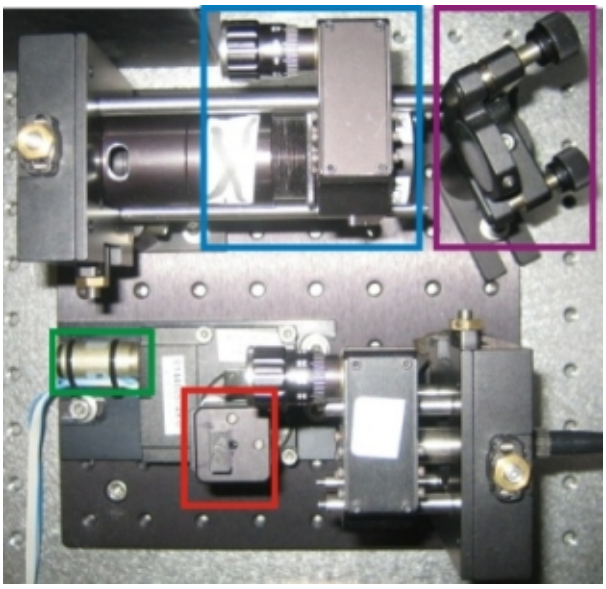

Figure 45: Actual picture of the spectrometer. Blue box: Lens with focal length, f=100mm in a tube holder with micrometer screw to adjust distance from fibre. Purple box: Mirror with spherical coordinate adjusting screws. Green box: stepper motor controlling grating postiion. Red box: Reflection grating on mount.

the zeroth order reflection back into the laser and other coupling inefficiencies. Also, referring to Figure 44, the full width half maximum (FWHM) of the He-Ne is measured to be 0.4 nm. Lasers have a much narrower line width compared to this, thus it is evident that this measurement is limited by the grating resolution, i.e. the resolution limit of the spectrometer is 0.4 nm.

3.4 Sample preparation

In this chapter, methods to cleaning coverslips and preparing samples will be introduced. This is the process whereby the molecules to be observed and the host matrix that holds the molecules in place are deposited onto the coverslip. Processes are carried out on a wet solvent bench. As this processes involve dangerous chemicals, safety wear should be donned at all times; lab coat, gloves and safety goggles. Safe disposal of these chemicals is also carried out by employing a waste disposal service rather than pouring the used chemical into the sink.

3.4.1 Coverslip cleaning

When attempting to image extremely small particles such as single molecules, it is crucial to ensure that the surroundings which the molecules reside are free from unwanted particles such as dirt or water droplets; as very sensitive detection will be used to detect very weak signals from the molecules, any brightly fluorescing dirt will easily be detected and mistaken as a fluorescent single molecule. Although having a clean

working environment is important, ensuring that the coverslips are clean during the preparation process is absolutely crucial to the potential usefulness of the sample. As the sample is coated onto the coverslip, any residual impurities present on the coverslip during the preparation process will be permanently embedded onto the sample.

To clean the coverslips, a chain of solvents is used to progressively wash away surface contaminants. At every one stage of the solvent chain, the coverslips are placed in a clean glass beaker filled with the particular solvent and everything is placed in a ultrasonic bath of 25 Hz to 45 Hz for 15 minutes. The successive solvents used are acetone, isopropyl alcohol and methanol in the said order. Acetone is used to remove organic compounds such as dust or dirt and isopropyl alcohol is used to remove non-polar compounds such as grease and oil. Lastly, methanol is used to remove the isopropyl alcohol. Methanol is highly volatile and evaporates quickly on its own. Ethanol can also be used to replace methanol.

After the solvent chain is completed, all coverslips are placed in a beaker of Pirañha solution until it is required to be used. The Pirañha solution consists of a ratio of two parts of concentrated 98% sulphuric acid (H_2SO_4) and one part concentrated 40% hydrogen peroxide (H_2O_2). The Pirañha solution derives its name from its ability of aggressively attack and dissolve organic molecules is also plays the role as a final organic contaminant removal solvent. When required to be used, a coverslip is removed from the Pirañha solution using a stainless steel tweezer. The coverslip is then rinsed with distilled water to wash away the Pirañha solution. The distilled water is then removed from the coverslip using a nitrogen air gun to blow the water off the coverslip surface. Finally, the samples are spin coated onto the coverslip.

There are other methods available in literature to clean coverslips, but this method is employed for its simplicity and availability of chemicals in the lab.

3.4.2 Host matrix

Two host matrices are used in the experiment, predominantly *p*-terphenyl, although PMMA/MA was also used in the initial phases of the experiment. Both host matrices are originally in the form of a white powder. Their solutions are prepared in the same way but different concentrations were used. For PMMA/MA, the resulting concentration was 20 mg/mL in toluene and for *p*-terphenyl it was 3 mg/mL in toluene. An ultrasonic bath for 30 min can also be performed to ensure homogeneity.

3.4.3 Fluorescent molecules

Terrylene comes in the form of shiny black powder in its pure form. To be able to deposit single molecules on the surface, it must be diluted down to an extremely low concentration. This is done by dissolving the terrylene powder into a toluene solvent. Generally, toluene dissolves most organic substances easily. A grain of terrylene powder of approximately 100 μm diameter is taken and placed into a small vial of toluene of roughly 10 mL. After which, the mixture is placed in an ultrasonic bath for about 30

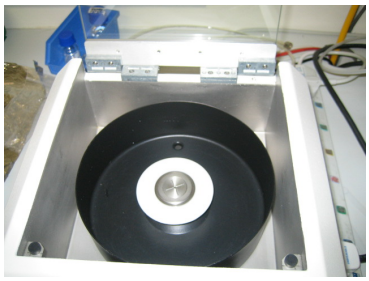

Figure 46: A picture of a spin coating machine, the coverslip is placed on the middle silver disk. Hole in the middle is connected to a vacuum pump and coverslip is held in place by vacuum during the spinning, in which the silver disk and the white collar disk spins at high velocity.

mins. The resulting solution should be evenly pink in colour and still transparent. Over time, the toluene may evaporate in storage, leaving the molecules behind in the vial, simply pour toluene back into the vial and perform an 30 min ultrasonic bath to restore the molecules into a solution.

3.4.4 Fluorescent beads

The fluorescent beads is originally a thick, bright pink coloured liquid. The beads are diluted using water in the ratio of 1 part bead solution to 10 parts water and spin coated on a coverslip. The resulting sample and concentration is shown in Figure 30.

3.4.5 Spin coating

In spin coating, a sample that needs to be deposited is placed on the coverslip by using a pipette. After which, the spincoating machine is programmed with the desired spin frequency and duration of spinning. Following from similar experiments found in literature [24], a spinning frequency of 1000 revolutions per minute (hereafter RPM) for 30 s followed by 3000 RPM for 2 s. The resulting thickness of the film is 20 nm [24].
To spin coat Fluorescent beads, the diluted sample can simply be placed on the coverslip. To spincoat the molecules however, the diluted terrylene solution has to be mixed with the host matrix solution first before spin coating. Firstly, extract a portion of the host matrix solution for use. The required concentration is so sparse that a needle is used by dipping the needle into the terrylene solution, taking it out of the terrylene solution and dipping it in a sample of the host matrix solution. The minute amount needed is the amount that is held by the surface tension between the needle surface and the terrylene solution.

4 Results and discussion

In this section, experimental data which are taken from the in-house built confocal microscope will be presented. Also, accompanying each set of results will be a discussion on the context in which the results are taken, and a short discussion in which improvements can be made.

4.1 Measured photon statistics

Before proceeding to discuss other results on single photon detection, a $g^{(2)}(\tau)$ function is first presented to confirm that single molecules and single photons are actually present in the experiment.

In Figure 47 is a normalized second order correlation function, or $g^{(2)}(\tau)$ function result from light emitted from a fluorescent terrylene molecule. The measurement is done using the Hanbury Brown and Twiss setup at irradiance of approximately 120 KW/m^2.

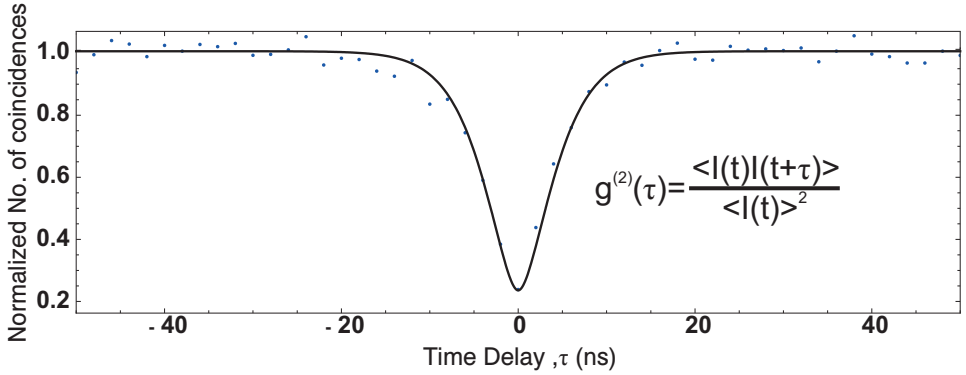

Figure 47: Second order correlation function, $g^{(2)}(\tau)$, of Terrylene in *p*-terphenyl host matrix using focused illumination of irradiance approximately 120 KW/m^2. Dots are actual data points, black line is best fit using equation 7. Curve is normalized to 1.0 at τ=∞, taken to be an experimental value of 50 ns.

Where the correlation function is normalized according to equation 9. Note that for the real data, $g^{(2)}(0) \neq 0$.This can be due to dark counts in the avalanche photodiodes currently used, or timing jitters for the clock doing the photon counting; such that photons arriving just before or after $\tau = 0$ is recorded as photon arriving at $\tau = 0$. However, so long as $g^{(2)}(0) < 0.5$ (see equation 2 and accompanying explaination), we can be certain that there is only one molecule in the observation focus and that light is still considered anti-bunched. Also, for real data, the correlation function is not normalized to true infinite delay time as indicated by equation 8. But it is normalized to realistic time delay of approximate order of magnitude in the microsecond range.

Also, one should take care to lower the excitation irradiance to roughly the range 120 KW/m^2 or lower if possible, as this would prolong the lifetime of the molecule from photobleaching and allow more photons to be collected.

4.2 Experiments with LED illumination

4.2.1 Spectral filtering

As the exitance spectrum from an LED is broadband, there is some difficulty in trying to filter the excitation light from the emission light. This represents a problem as the excitation light can actually be reflected off the glass coverslip due to Rayleigh scattering in addition to unwanted background fluorescence [16, 13]. These undesirable light then propagate back into the detection path. Thus, there are three components in the light emitted by the sample; the back reflected illumination light, the legitimate molecular fluorescence and the background fluorescence. Removing the illumination light component is not a problem for lasers, for lasers only has a very narrow spectral bandwidth and easily filtered off by the dichroic mirror or a High pass filter.But for LEDs, the broadband emission means that the back reflected light is also broadband and can be transmitted through the dichroic mirror and high pass filters. As background fluorescence induces a red-shift in the scattered light with respect to the incident light, eventually some of this scattered light might be transmitted through the dichroic mirror and reach the detectors. This reduces the signal to background ratio as the scattered light becomes indistinguishable from real fluorescence. Usage of quartz coverslip is also recommended in for lesser fluorescence [13], but is not available for this experiment. This is concept is illustrated in Figure 48.

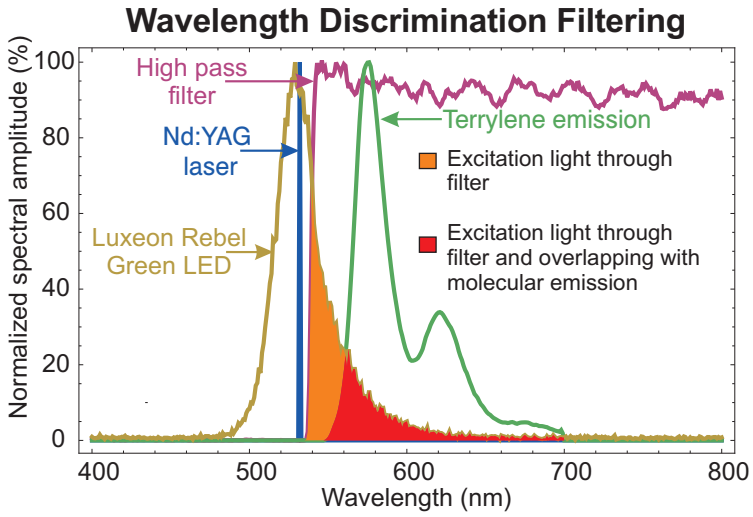

Figure 48: Cutting off excitation light from being detected is easier with the laser than with the LED. This is especially true for the red shaded region; it can be indistinguishable from legitimate fluorescence and contributes to background signal. Also, cutting off this light will compromise legitimate molecular emissions.

Of the many filters available in the lab, there needs to be a way to find the optimum filter to use in conjunction to the light emitted from the molecules and the light from the LED. To facilitate in the selection of the optimum filter function, the transmission spectra of all filters are scanned using a Perkin-Elmer Lambda 950 spectrometer. Subsequently, to calculate the most efficient illumination filter for the LED, a numerical calculation is performed with the software Mathematica in which the expression:

$$\int l(\lambda)[\prod f(\lambda)]a(\lambda)d\lambda \tag{45}$$

yields the largest numerical value for different sets of filter transmission spectrum, $\prod f(\lambda)$. Where $l(\lambda)$ describes the excitation source emission spectrum and $a(\lambda)$ describes the absorption spectrum of the molecules. $l(\lambda)$ can either be the LED or the laser spectrum. The largest value will then correspond to the best spectral efficiency when exciting the molecules. After comparing the various filters, the following one yields the best overlap with the LED and the molecular absorbtion, the Photonik bandpass filter, shown as "BP500580" in Figure 49. The absorption spectrum is measured by putting a concentrated sample of molecules suspended in liquid solvents held by quartz cuvettes into the Perkin-Elmer Lambda 950 transmission spectrometer. The emission spectrum is then the mirror image but offset by the Stokes shift, as shown in Figure 2.

A corresponding calculation is also performed with the emission and detection arm of the confocal microscope. This is shown in Figure 50 by evaluating equation 46

$$\int e(\lambda)[\prod f(\lambda)]d\lambda \tag{46}$$

Where $e(\lambda)$ is the molecular emission spectrum.

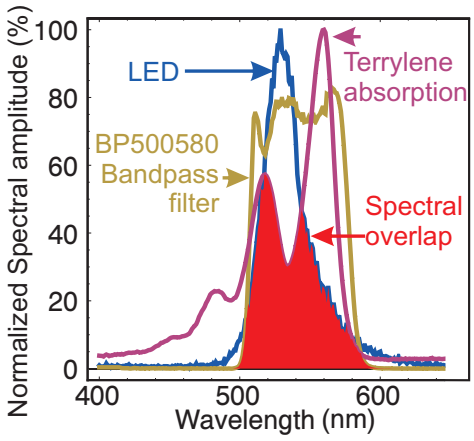

Figure 49: Exciter filter with the best spectral overlap with absorption spectrum of Terrylene. Here we assume that the reflection bandwidth of the dichroic is infinitely broad. Evaluating equation 45 will yield a 30% of LED power being incident on molecules.

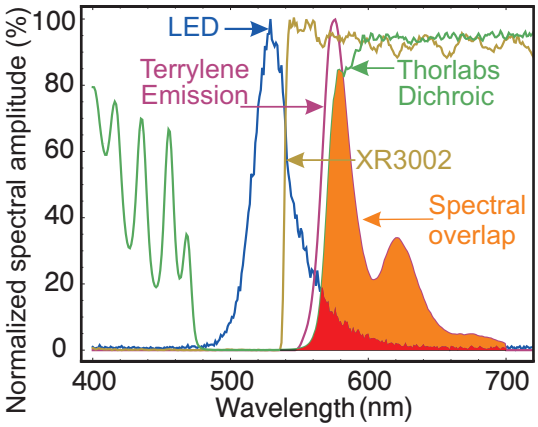

Figure 50: Detector high-pass filter with the best spectral overlap with emission spectrum of Terrylene. The orange portion denotes the signal from the molecular fluorescence and the red region denotes the background contributed by the LED. Evaluating equation 45 will yield a 70% fluorescent light reaching the detectors.

However, although they produce the most efficient transmission of the LED light and the best detection of fluorescence light individually, their combined usage is not favorable as a relatively large portion (3%) of the **filtered** LED light leaks through the dichroic mirror and high pass filter to reach the detectors; which can be easily detected

in sensitive detection. This is shown in Figure 51.

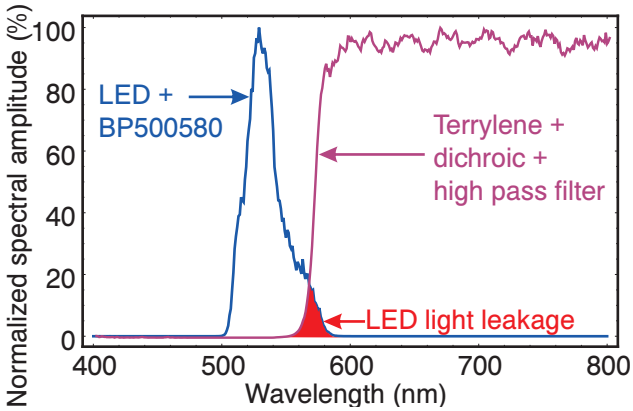

Figure 51: Individually optimal filters for detection and emission arms of the confocal microscope may not yield the best result.Red portion denotes protion of light that still enters detectors. Blue line is the spectrum of filtered light using the Photonik BP500580 and purple line is the combined transmission spectrum of the Thorlabs dichroic AND the XR3002 high pass filter. The red shaded region denotes 3% of the LED light leaking through the high pass filter and dichroic mirror.

Note that Figure 51, the peak amplitudes of the plots are normalized to 100% as potraying the profiles is the main aim of the figure. As seen in Figure 51, any attempts to shift the high pass filter to the a higher cut off wavelength will further attenuate legitimate signals from the fluorescent molecules. Moving the bandpass filter to a lower wavelength band will also cut off the frequency components that overlap with the terrylene dominant absorption wavelength. Thus, both situations are unfavorable. In section 4.2.5, the ideal filter cutoff frequency for both filters will be calculated.

4.2.2 Spectral coverage of LED

Apart from its low cost and compactness, the broadband emission of an LED also means that the spectral overlap of the LED is superior to that of a laser's narrowband spectrum. If we set:

$$\int l_{\mathrm{LED}}(\lambda)[\prod f(\lambda)]d\lambda = \int l_{\mathrm{laser}}(\lambda)[\prod f(\lambda)]d\lambda \tag{47}$$

where $l_{\mathrm{LED}}(\lambda)$ is the emission spectrum of the LED, $l_{\mathrm{laser}}(\lambda)$ is the emissions spectrum of the laser and $\prod f(\lambda)$ is the product of all filter transfer functions, including that of the dichroic mirror. Thus, $\int l_{\mathrm{LED}}(\lambda)[\prod f(\lambda)]d\lambda$ is the irradiance on the molecules due to LED excitation, $\int l_{\mathrm{laser}}(\lambda)[\prod f(\lambda)]d\lambda$ is the irradiance on the molecules due to laser excitation. Using Mathematica to perform numerical analysis, we are able to have a 38% in power available to the molecule. This concept is illustrated below in Figure 52. Note however, for sake of clarity, conditions describe by equation 47 is not represented in Figure 52; i.e. the laser and LED powers are not the same in this case, but both spectral amplitudes are normalized to one.

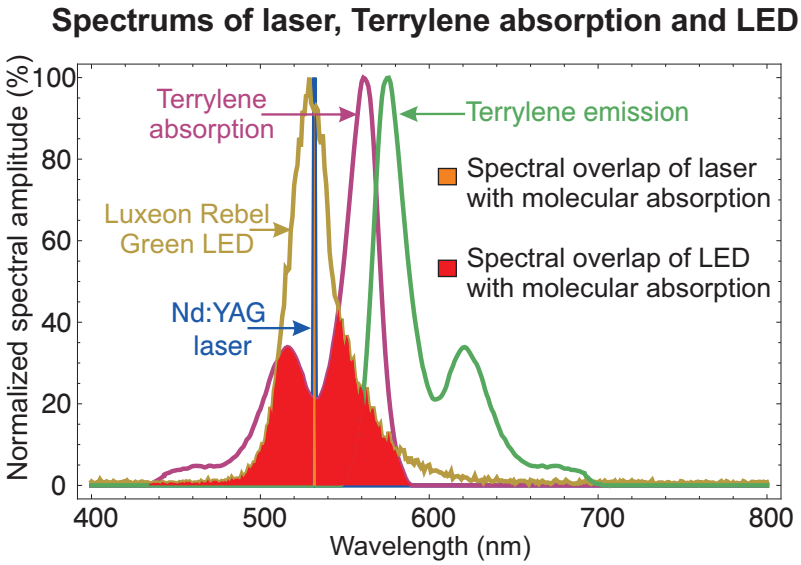

Figure 52: Higher spectral overlap and more efficient excitation for LED. Note that peak absorption wavelength is covered by the LED emission. Further note that this graph does not contain filtering or reflect the scenerio whereby both LED and laser have the same irradiance, that would have laser spectral amplitude too high to be graphically displayed. Thus, the two graphs are normalized to spectral amplitude of one.

4.2.3 Surface irradiance of laser and LED

By using the CCD camera, and slowly decreasing the laser irradiance using a neutral density filter in widefield mode, we are able to determine that the smallest optical power needed to observe single molecules on in the CCD camera is 11μW. The illuminated area is a circle of diameter approximately 13 μm^2. This corresponds to an irradiance of 83 KW/m^2 required to see single molecules. This is using a camera gain of 38dB and a long integration time of 10.24 seconds (256 frames).

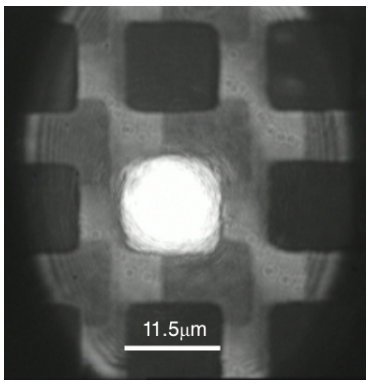

Figure 53: Measuring the widefield spot using a TEM grid, diameter is determined to be approximately 13 μm^2. Note the slight illumination beyond the lighted square. Illuminated area is slightly bigger than the square; this is observable by moving the spot around and to the other squares.

A high pass filter is placed before the CCD camera, the filter used was an Omega XR3003 high pass filter tilted to an angle where the illumination light is just filtered off . The cut off wavelength of the filter transmission spectrum can be calculated using [40]:

$$\lambda(\theta) = \lambda_0 \sqrt{1 - [\frac{sin(\theta)}{n_{\text{eff}}}]^2} \tag{48}$$

Where $\lambda_0 = \lambda(0)$, θ is the angle of incidence and n_{eff} is the effective refractive index and is polarization dependent.

Measuring the irradiance of a focused laser beam is easier compared to the LED, as the radiant flux of the laser can be measured at any point of the beam prior to entering the objective lens by simply putting the photodiode as the illumination laser path. An assumption of zero loss can be made with regards to the transmission of the microscope objective lens and a lossless propagation of the laser in air. The illuminated laser area can be ascertained on screen, as seen in Figure 53 for widefield illumination, or using equation 13 for focused illumination. The LED offers no such advantage. With the LED, the high divergence of the source makes it difficult to measure such a value accurately. The area illuminated by LED light on the sample is also large compared to the small focus of a laser beam; and this area is difficult to measure. Thus, it is not possible to use the above technique to measure and calculate the LED irradiance. The LED light is collected by using a NA 0.68 aspheric lens placed before the LED and directed forward by using a f=50 mm lens.

By using fluorescent beads, we are able to vary the laser irradiance in widefield mode until the bead fluorescence between the LED and the laser are comparable. This allows us to detect the LED irradiance on the sample. By using Fluorescent beads, the irradiance provided by the LED is determined to be approximately 15 KW/m^2; which is 5.5 times lower than the minimum laser irradiance needed to see single molecules on the CCD camera, 83 KW/m^2. Also, the LED illumination suffers from significantly poorer signal to background ratio due to the broad band emission of the LED. As will be explained in greater detail in the section 4.2.1.

As mentioned above, using a laser illumination in widefield mode, we are able to observe molecular fluorescence using a CCD camera at 83 KW/m^2, that is $I_{\text{min-laser}}$=83 KW/m^2. Since the Nd:YAG laser has a defined wavelength of 532 nm and that:

$$E_{\text{photon}} = \frac{hc}{\lambda} \tag{49}$$

Where h is the Planck's constant in eV, 4.135667 $\times$ 10^{-15} eV s, c is the velocity of light in vacuum, 2.99792 $\times$ 10^8 m/s and λ is the wavelength of light having the energy, E_{photon}. Then this would correspond to photons of energy, E_{photon} 2.332 eV or 3.735 $\times$ 10^{-19} J and a photon density, ρ_{photon} of,

$$\rho_{\text{photon}} = \frac{I_{\text{min-laser}}}{E_{\text{photon}}} = 2.22 \times 10^{23}/m^2 \tag{50}$$

Knowing that the molecule, terrylene, has a absorption cross section of σ_{ab}=7 $\times$ 10^{-16}cm^2 [16] and a quantum efficiency, η=1.0 [20], this would mean that the absorption and re-emission rate is

$$\Gamma_{ab} = \sigma_{ab}\eta\rho_{\text{photon}} \approx 15000\ second^{-1} \tag{51}$$

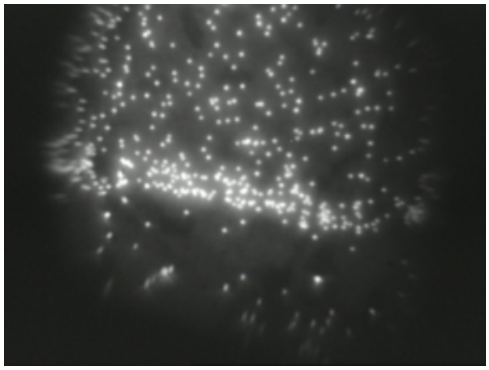

(a) A picture of an LED illuminated Fluorescent beads. Used a condenser consisting of f=25 mm and f=3.1 mm lenses.

(b) Picture of laser illuminated Fluorescent beads by decreasing the laser radiant flux to give the same level of fluorescence as the LED picture in Figure 54(b). Note the same bead pattern in the same illuminated area in Figure 54(b).

Figure 54: Measuring LED irradiance on sample surface.

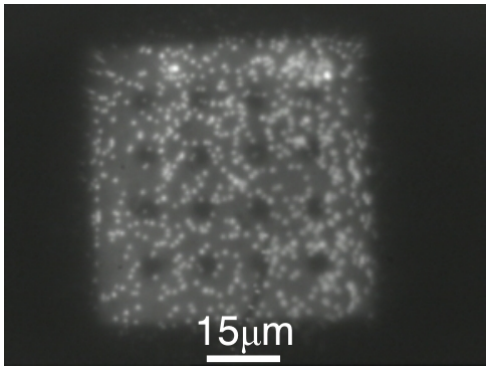

(a) A picture of an LED die imaged onto a sample of Fluorescent beads. Unlike Figure 54(a), a single f=50 mm lens is used before the LED, this makes the die features visible.

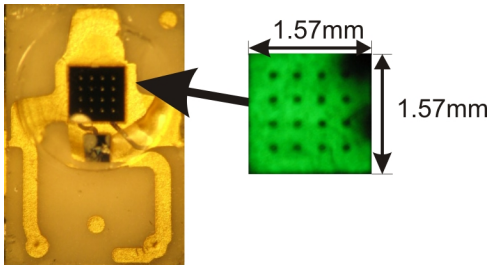

(b) Picture of LED die.

Figure 55: Picture of LED imaged onto Fluorescent beads

That is, 15×10^3 photons are absorbed and re-emitted by the molecule every second. Further assuming that the detection efficiency of the microscope is only 1% (a comparable but more conservative estimate compared to similar experiments found in literature [16, 11]), due to various filtering losses or inefficient light collection by the microscope objective, then only 156 photons can be detected by our APDs. Considering our APD dark counts are about 150 counts per second, the signal to background ratio is only about 1, bearing in mind that this is the bare minimum irradiance required to observe single molecules. Using an APD can also improve the detection sensitivity of fluorescent light such that we may even be able to operate below the critical value of, $I_{\text{min-laser}}$.

By applying a same analysis to the LED irradiance, by just changing $I_{\text{min-laser}}$ in the calculations to I_{LED}=15 KW/m^2. The result will show that the detectors will read 28

photons per second, which is below the dark count and thus impossible to read; with a signal to background ratio of 0.2.

To compute the upper bound irradiance on the sample surface, an assumption is made that the maximum irradiance occurs when the LED exitance is fully transferred from the LED die surface to the irradiated sample surface. This is calculated using die area of 2.456 mm^2 given in Table 1 and the LED optical output power of 300 mW when the LED is overdriven at 1.5 A as shown in Figure 40.

$$I_{\text{LED-exit}} = I_{\text{sample}} = \frac{300\ mW}{2.465\ mm^2} = 121\ KW/m^2 \tag{52}$$

This would then indicate that the irradiance, even when under ideal conditions without taking into account filtering and other divergent losses is only 1.5 times above the minimum irradiance required to see fluorescent single molecules on a CCD camera. Comparing this to the measured irradiance on the sample surface, 15 KW/m^2, the eventual irradiance by the LED on the sample surface is only about 10% of the original LED exitance. Probably due divergent losses due to the inability to collimate incoherent light from the LED. Thus, although the radiant flux of the LED is high, the intensity, exitance and subsequent irradiance is low.

4.2.4 Signal to background ratio of laser and LED

Using the CCD camera, we are able to observe single molecules on the sample surface easily with a laser, with relatively high signal to background. Using the flippable mirror, we are also able to easily switch to the LED illumination mode (see Figure 25). Thus, we are able to compare between the two illumination schemes. This is shown in Figure 56 with their corresponding profiles at the side. The profiles are generated by taking images using the CCD camera for both illumination modes at the same illuminated location. After which the images are processed using Mathematica and selecting cross section profiles. Objects are concluded to be single molecules due to the observation of blinking and single step bleaching. A second order correlation function has not been measured for LED illumination as the poor signal to background ratio makes such a measurement impossible.

Just by inspection, one can ascertain from the profiles that the signal to background ratio of the laser illuminated sample is higher than that of the LED illuminated sample. The LED illuminated sample is plagued by a high background due to background fluorescence of the coverslip, probably attributed to background fluorescence of incident broadband LED light off the coverslip glass. The pictures are taken using a brand of coverslips named "Cellpath", changing to the Fischer Scientific coverslips yielded less background fluorescence. At the end of the project, a premium range of Fischer Scientific coverslips have been ordered and yet to arrive from shipping. In literature, there exist more elaborate methods of coverslip cleaning [13, 41] which require more chemicals that are not available in the lab. Problems with using glass coverslips are also documented in literature [16, 13].

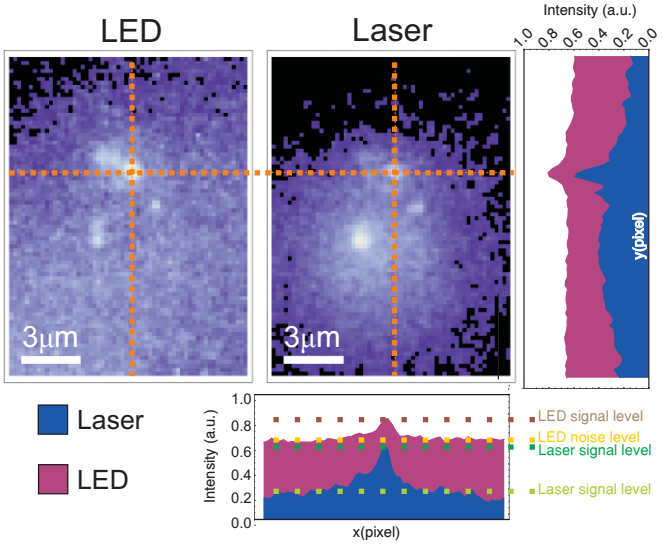

Figure 56: Fluorescent molecules illuminated by an LED and with a laser of comparable irradiance at approximately 15 KW/m^2. Note that the laser is always able to produce a higher signal to background ratio .

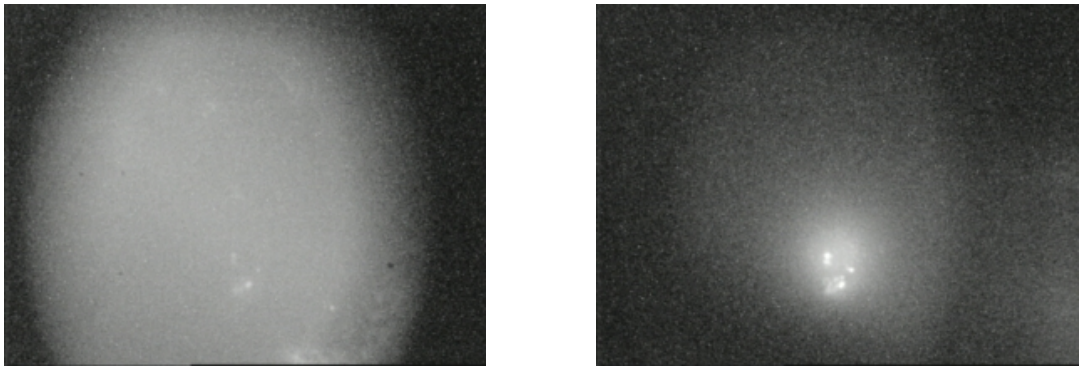

(a) A picture of fluorescent molecules illuminated with a LED.

(b) Same area as a) but that a laser is used in wide-field mode.

Figure 57: Pictures of LED and laser illuminated fluorescent samples, identified via blinking and single step bleaching. Note the difference in signal to background ratio.

In Figure 59, it is shown that the confocal scan using a focused illumination beam gives a higher signal to background ratio of 17.3, which is comparable to similar setups reported in literature [16]. Note that the colours denote exitance, not true colours as depicted by the eye.

Eventually, it was discovered that the toluene used in the experiment is contaminated with unknown fluorescent molecules. This conclusion is derived from spin coating toluene on a coverslip and putting the coverslip under the microscope. The toluene coated coverslip displayed strong background fluorescence and even some single fluorescent molecules that exhibited single step bleaching. Placing a cleaned coverslip under the microscope showed reduced background fluorescence, which showed that the problem was caused by the toluene.

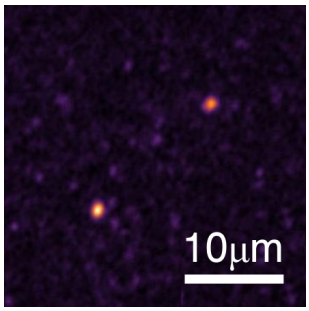

Figure 58: Fluorescent terrylene molecules imaged by confocal scan with illumination irradiance of approximately 150 KW/m^2. Signal to background ratio is approximately 17.3.

Thus, in principle we are able to observe single molecules using an LED, however, the signal to background ratio remains very low and would hinder measurements of a second order correlation function. Also, only very bright molecules can be observed, dimmer molecules are easily drowned out by the background fluorescence.

4.2.5 Ideal filter

By comparing the spectrums, the ideal filter can be calculated as a pair of filters, one at the LED and the other at the detectors, which will allow for the excitation of the comparable absorption of the LED light by the molecule, and the transmission of fluorescent light while blocking the LED light from reaching the detectors. These two filters, when placed together, should not allow any light through. By modelling the high pass filter placed before the detector as a unit step function,

$$u(\lambda - \lambda_c) \tag{53}$$

Where λ is wavelength and λ' is the cut off frequency of the ideal high pass filter, then the low pass filter placed before the LED is automatically have the same cutoff wavelength and a filter transfer function of:

$$1 - u(\lambda - \lambda_c) \tag{54}$$

To find the cut off wavelength of the filters that will yield the best LED light absorption by the terrylene to emission detection, Mathematica can be used to process the equation

$$\Delta P(\lambda, \lambda_c) = \left| \int_{400}^{\lambda_c} l(\lambda)a(\lambda)\, d\lambda - \int_{\lambda_c}^{800} e(\lambda)\, d\lambda \right| \tag{55}$$

Where $l(\lambda)$ is the LED spectrum, $a(\lambda)$ is the absorption spectrum of the molecule and $e(\lambda)$ is the spectrum of the molecular fluorescence. The operating wavelength

range is taken to be between 400 nm to 800 nm. A minimum value of $\Delta P(\lambda, \lambda_c)$ will mean that the emission of the molecule and absorption of LED light by the molecule is comparable. A plot for $\Delta P(\lambda, \lambda_c)$ is shown below and cut off wavelength in which the minimum value occurs is calculated to be 565 nm.

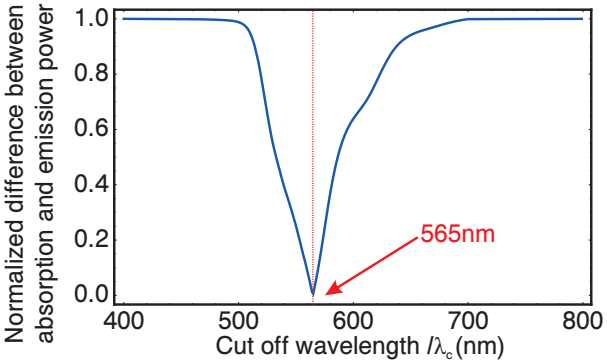

Figure 59: Difference between absorbed power and emitted power as a function of filter cut of, the least difference indicates the most comparable emission and absorption.

4.2.6 Modal filtering

Since it is impossible to focus incoherent light down to a single spot, irradiance is then compromised as a given amount of optical power is now spread across a large area. One method is to perform spatial filtering of light to obtain a single mode of light with a Gaussian profile. This is done by placing the LED before a condenser composing of two high NA aspheric lenses which captures and focuses the light into a single mode fibre. The two aspheric lenses used have a NA of 0.68 for the lens near the LED and a NA of 0.25 for the lens collecting the light into the single mode optical fibre; as the single mode fibre has an NA of approximately 0.12, any lens used to focus light into the fibre with a lens NA higher than the NA of the fibre would not have any increased collection effect as compared to using a lens with a NA matching the NA of the fibre. Since the single mode fibre can only accommodate a single mode, only one mode of light propagation will emerge from the other end of the optical fibre. This light can then be collimated and focused just like a laser beam as it now a Gaussian beam. Thus, the end of the fibre is connected to the confocal microscope and used in place of the Nd:YAG laser. By measuring with an avalanche photodiode, the output optical power from the optical fibre is measured to be 4nW from an original optical power output of 250 mW from the LED. That is, let P_{smLED}=4nW. Such high losses are expected in filtering only one mode from the LED source.

Now that the light can be filtered down to a diffraction limited spot, with area

$$A = \pi(0.61\frac{\lambda}{NA})^2 \tag{56}$$

And as mentioned earlier the minimum intensity required is $I_{\mathrm{min\text{-}laser}}$=83 KW/m^2, the

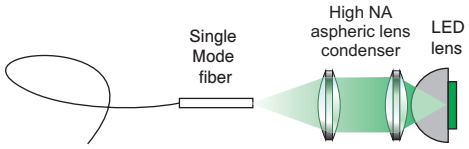

Figure 60: Using a single mode fibre to extract a single Gaussian profile from the LED.

critical minimum area that the 4nW single mode LED light must have is also

$$A_{\text{crit}} = \pi(0.61\frac{\lambda_{\text{crit}}}{NA})^2 = \frac{P_{\text{sm-LED}}}{I_{\text{min-laser}}} \tag{57}$$

$$\therefore \lambda_{\text{crit}} = \sqrt{\frac{A_{\text{crit}}(NA)^2}{\pi(0.61)^2}} = \sqrt{\frac{P_{\text{sm-LED}}}{I_{\text{min-laser}}}\frac{(NA)^2}{\pi(0.61)^2}} = 285.25nm \tag{58}$$

Where the NA of our objective lens is 1.4.

Thus from the equation 58, only light with wavelength lesser than 285 nm can be focused down to a diffraction limited spot with sufficient irradiance to observe molecular fluorescence on a CCD camera. As seen from Figures 48,49 and 50, the LED has a spectrum in the range much larger than 285 nm; thus, this is theoretically impossible due to low irradiance.

A confocal scan using the spatially and spectrally filtered light remains inconclusive as no single molecules are detected. This is probably due to the broad band emission of the light that is still incident on the glass coverslip.

4.3 Reprogrammed piezo stage

The confocal microscope setup was inherited from a previous PhD student working with quantum dots and modifications have been made to the tomography raster scanning Tcl/Tk program that came with the microscope which controls the piezo stage. One of the modifications is to automate the molecule location process. Now the program will be able to automatically locate the brightest spot and position the suspected molecule under the microscope objective lens for observation. This feature is activated by selecting the radio button "`gomax`" shown in Figure 62. The piezo stage program is also able to detect the single step bleaching of molecules and search for the next single molecule within the sample. A similar test is ran with Fluorescent beads and this is shown in Figure 61, note that the beads take much longer to photobleach; whereas the molecules lasts a few minutes on average, beads can last for hours and their exitance decreases gradually instead of in a single step.

As molecules also undergo dark state blinking, it is also possible to specify the duration the program can wait before searching for another bright spot. It will hold the sample there for a small amount of time and read the fluorescence again. This

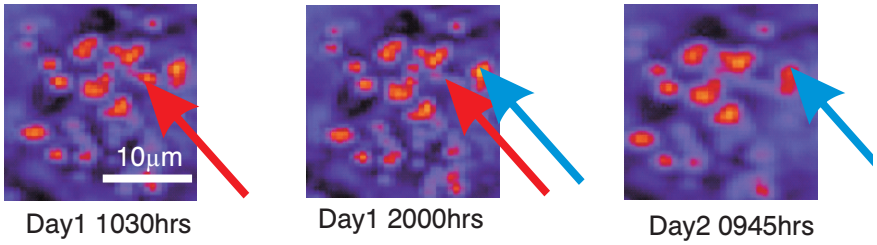

Figure 61: piezo stage program running for 24 hours continuously on a sample of Fluorescent beads under constant focused illumination. Beads take much longer to photobleach. Arrows show the areas where photobleaching has occurred and this proves that the program is a capable of searching for molecules autonomously. Colour of arrows shows reciprocal sites across pictures and their corresponding photobleaching.

hold time is specified by "`Blink time threshold (ms)`" in Figure 62. If the reading is still low, the program will determine that the molecule is bleached and move on to find another molecule. If the reading is high again, the photon collection goes on per normal. Usually, a 1 ms delay time is used as from experience, the blinking effects are less than 1 ms. Similar phosphorescence effects reported in literature have shown the triplet state lifetime of terrylene in *p*-terphenyl to be 18 ± 2 μs [16]. The critical value which the program will use to judge if a molecule is present can be specified in the "Minimum count threshold" in Figure 62.

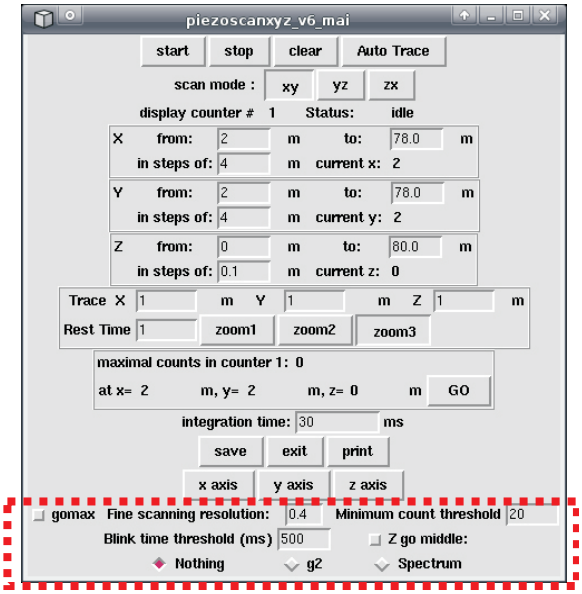

Figure 62: A picture of the GUI used to control the piezo stage. Red box indicates the additional features added by me. Radiobutton "gomax" sets the program to seek out the maximum exitance. Fine scan tells the program how high a resolution it should scan to search the exact position of the molecule.

To save scanning time, the program first does a fast rough scan with low resolution, then goes to the region of the highest exitance and performs a fine scan to finally locate the exact spot of highest exitance. The program then positions that spot under the microscope objective. The fine scan resolution is defined in the box labelled "`Fine scanning resolution`" in Figure 62. A lower value keyed into this box will result

in a longer scan time but more accurate positioning

Finally, "`Z go middle`" is used to move the piezo stage to the middle of the Z scan range specified in the Z "from" and "to" fields. This allows us to scan through the focused plane so we can get successive cross section slices of the sample.

All the while, the program will output the status of the program to the command line. Another program will be running in the background and monitoring the command line for a message stating that a molecule has been located and is now being held in the objective lens focus. Upon this happening, the background program will launch another program which actually starts measuring the second order correlation function.

A flowchart of the program can be found in Figure 69 in the Appendix.

5 Conclusions

5.1 Summary

In this experiment, an existing confocal microscope was modified for use on an vibration-damped optical table. Simple opto-mechanical structures were build using s CNC machine as a part of a redesign of the confocal microscope. The confocal microscope is able to perform its normal task by acquiring widefield images with the CCD camera and confocal images of single molecules with high signal to background ratio. The scan program written in Tcl/Tk is also further modified by making it look for molecules autonomously. By using APDs in the Hanbury Brown and Twiss detection scheme, the microscope is made to be single photon sensitive and clearly demonstrated the capability to detect anti-bunched photons emitted from a single molecule by the measurement of a second order correlation function. Strong anti-bunching is clearly resolved as expected form emission by a single molecule. Single terrylene molecules are embedded into host matrices of *p*-terphenyl and PMMA/MA by the use of spin coating techniques and carried out on a chemical solvent wet bench. A spectrometer is also attached to the confocal microscope and is capable of measuring the spectrum of light using an APD as a detector.

A break from reported literature is attempted with switching the illumination source from a traditional laser source to an incoherent light source in the form of an LED. A LED cooling system is also developed to drive LED at currents higher than the datasheet values. Under LED illumination, single molecules are visible intermittently but only by observation of single step bleaching, which is a characteristic behavior of single molecules. Drawback of using an LED light is low intensity and irradiance due to the large LED die size, notwithstanding high radiant flux of an LED. Spatial incoherence also prevented the light from an LED from being focused onto a small focus of high irradiance as would be easily possible with laser light. Broadband emission from an LED source also meant that spectral filtering would be a problem. This means a high background is observed by the detectors as illumination light is inefficiently filtered. Spectral analysis is also performed to find the best filters for the experiment, including a numerical analysis to find the ideal cut off wavelength.

5.2 Outlook

An important goal would be to measure the second order correlation function of single molecules using LED light. Something that has not been reported in literature. Although single molecules have been identified through their single step bleaching behavior, this is not the most rigorous determining yardstick for measuring the presence of a single molecule.

As aforementioned, the experimental problems that are encountered are mostly attributed to contaminants in the chemicals used and poor quality glass coverslips. One way forward is to order a fresh batch of chemicals that are free from contaminants. Another alternative that can be explored is to use quartz coverslips as done so by other

groups which is reported to have less background fluorescence [13].

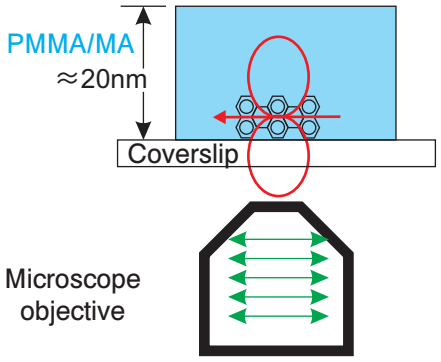

Figure 63: Transition dipole moment of a terrylene molecule in PMMA/MA. Emission now directed towards objective lens.

Another idea that can be pursued is to use PMMA/MA host matrix again instead of *p*-terphenyl. As shown in Figure 3 in section 2.1.1, the transition dipole moment in of terrylene in *p*-terphenyl has a defined transition dipole moment which points in the longitudinal direction of the illumination laser. This means that absorption and subsequent fluorescent emission of the terrylene molecules is less efficient compared to a situation where the terrylene transition dipole moments are lying flat on the coverslip as the illumination beams have polarization directions in the plane transverse to the direction of propagation, as shown in Figure 63; molecular absorption is most efficient when transition dipole moment of the molecule and polarization of the light are parallel. Although PMMA/MA does not guarantee that the molecules will be aligned lying flat onto the coverslip and hence, have transition dipole moments lying on the transverse plane of the illumination light, it does allow a high probability of it happening as PMMA/MA does not force the transition dipole moment to lie in a pre-defined orientation [24]. Also, since the molecule has a dipole antenna profile emission pattern (emitting to the side), having the transition dipole moments lying on the coverslip also implies that the side way emission will be directed at the microscope objective and fluorescence photons can be collected more efficiently, giving a better signal to background ratio.

However, using PMMA/MA means that it is not possible to take advantage of the photo and spectral stability offered by crystalline matrices such as *p*-terphenyl.

Also, a customized filter set can be purchased with the specification close to the one proposed in section 4.2.5.

Apart from terrylene, other quantum emitters can also be studied using the modified confocal microscope. Such as colour-centered diamonds [10], fluorescent protein [12], rhodamine family of dyes [12], dibenzoterrylene or CdSe colloidal quantum dots just to name a few. In particular, molecules which have an absorption spectrum in the long wavelength regions, as red LEDs tend to have a better conversion efficiency and thus, a higher irradiance.

Also, other experiments that have previously been done by pulsed lasers can now be attempted with LEDs [9, 14]. One of which is to be able to generate single photons on demand; the probability of generating only one photon with every pulse is up to 88% with a laser [9] and it would be interesting to see if this process can be increased to a higher efficiency.

6 Acknowledgement

First and foremost, I would like to thank and acknowledge the invaluable help offered to me by Dr. Ilja Gerhardt. His patience and guidance has been indispensable in this project and my education.

Also, this work will not be possible without the kind acquiescence of Dr. Antía Lamas-Linares and Dr. Aaron Danner in supervising my research. My stint would also not have been possible without the permission and sponsorship of Dr. Christian Kurtsiefer.

I would also like to acknowledge the work and collective knowledge of the previous project group consisting of Dr. Gleb Maslenikov and Mr. Tey Meng Khoon who worked with colloidal quantum dots using the confocal microscope, that I now use. Their pioneering efforts made my current work possible.

Mr.Gan Eng Swee's help around the workshop was also instrumental in helping me with technical work.

Lastly I would also like to thank both the Quantum Optics group at the Centre of Quantum Technologies and the Centre of Quantum Technologies as a whole for sponsoring and financing my research.

Appendices

A Technical drawings

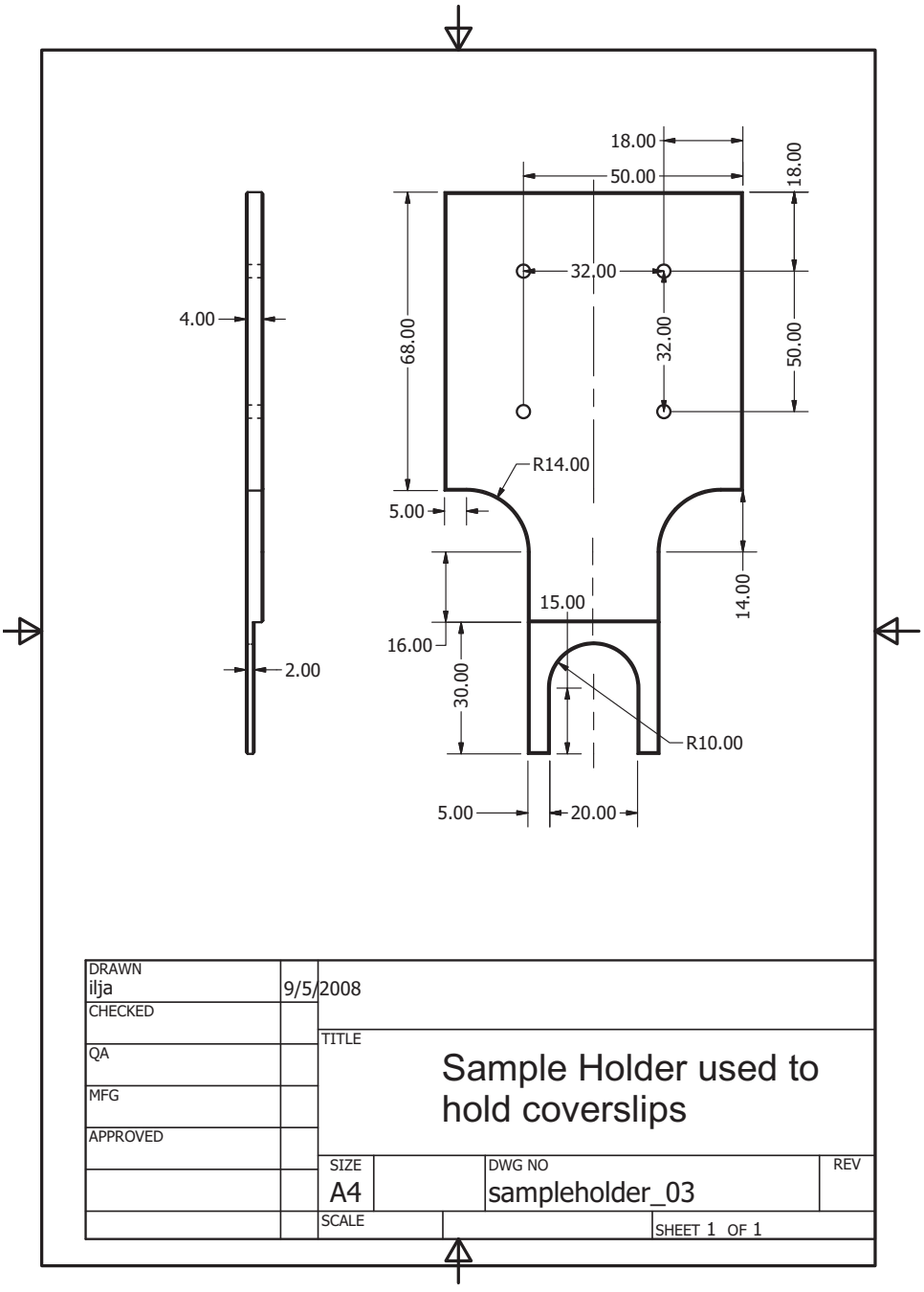

Figure 64: Drawing of sample holder.

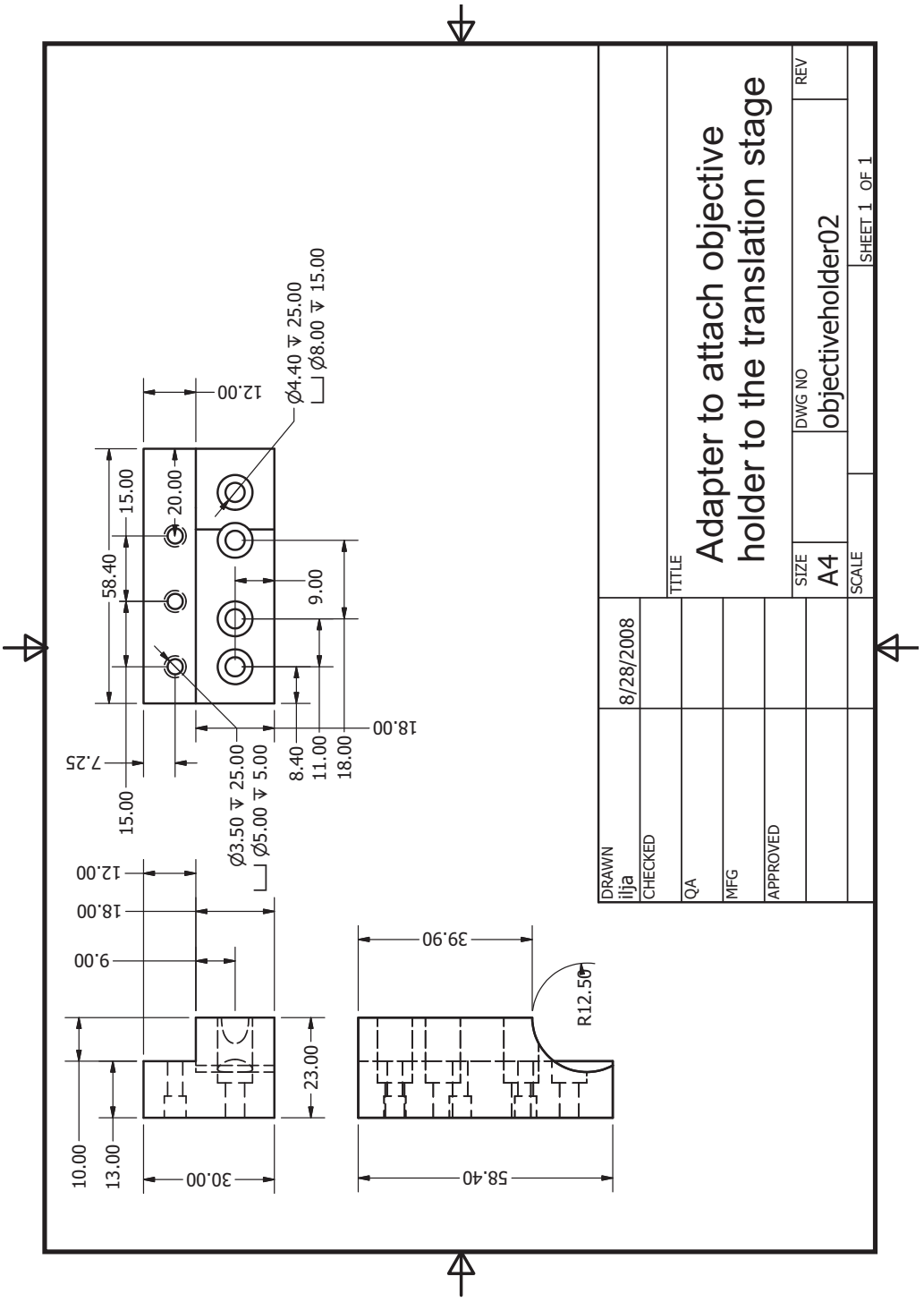

Figure 65: Drawing of objective adapter.

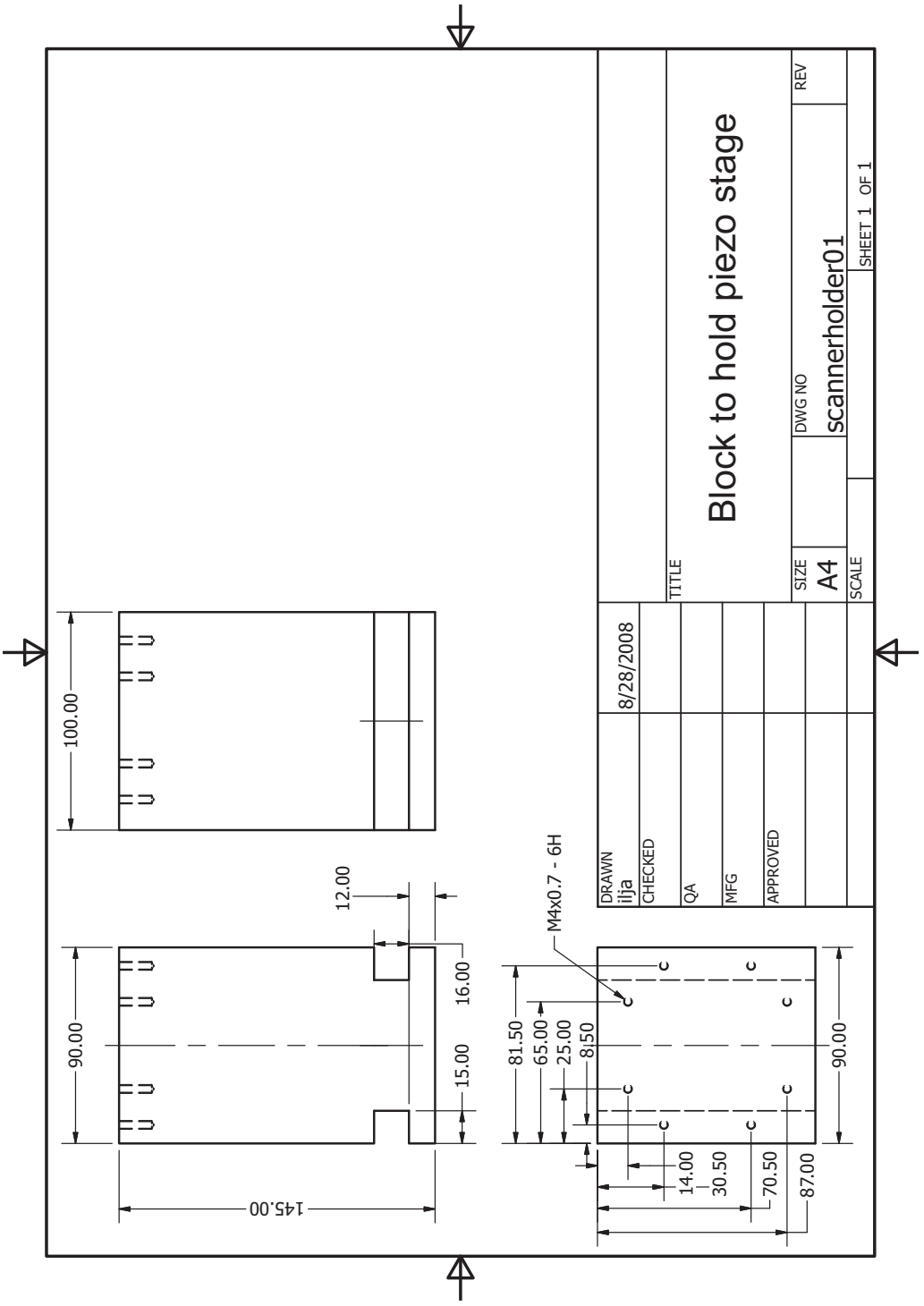

Figure 66: Drawing of red block which holds the piezo scanner.

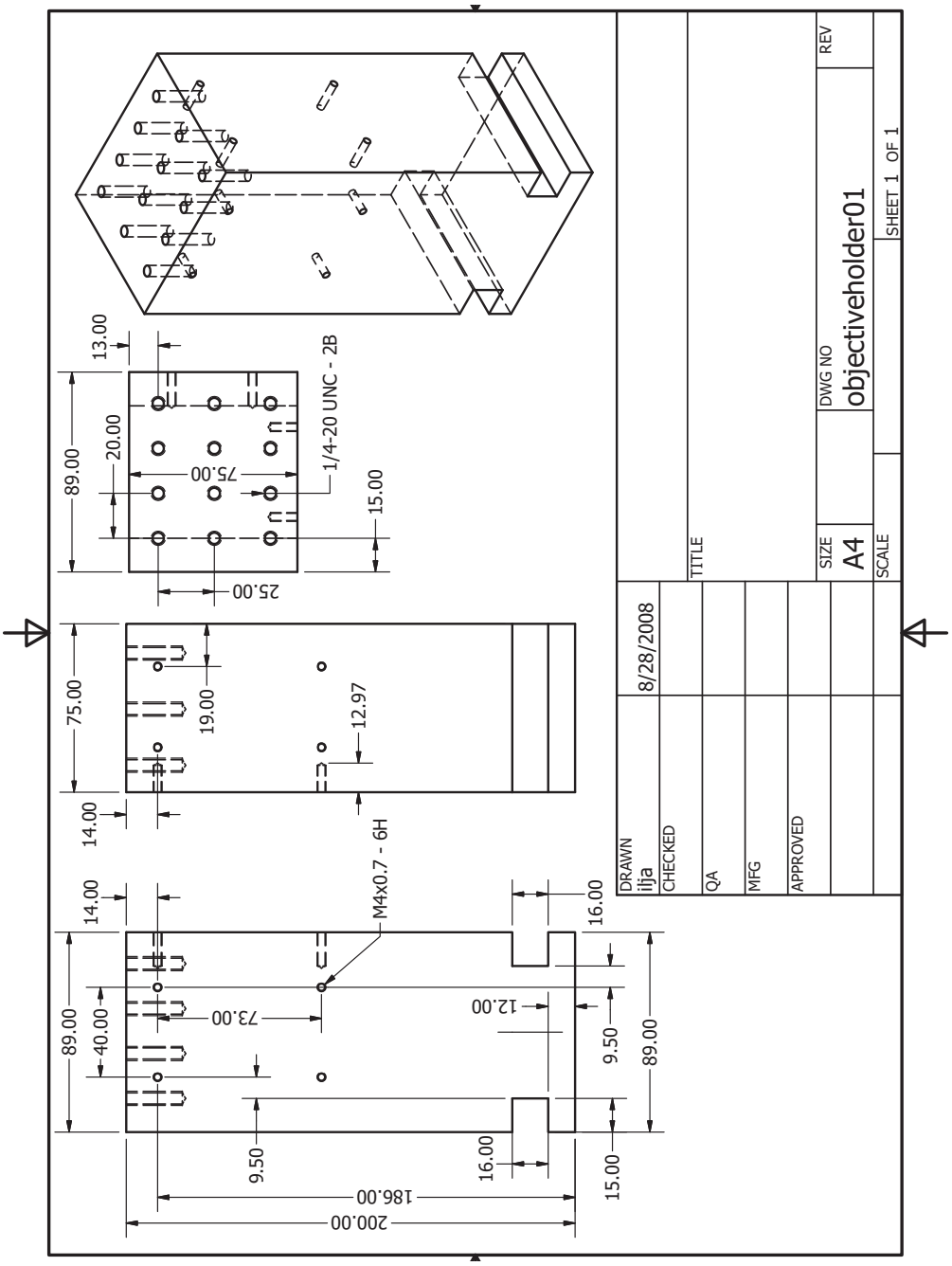

Figure 67: Drawing of red block which holds the objective.

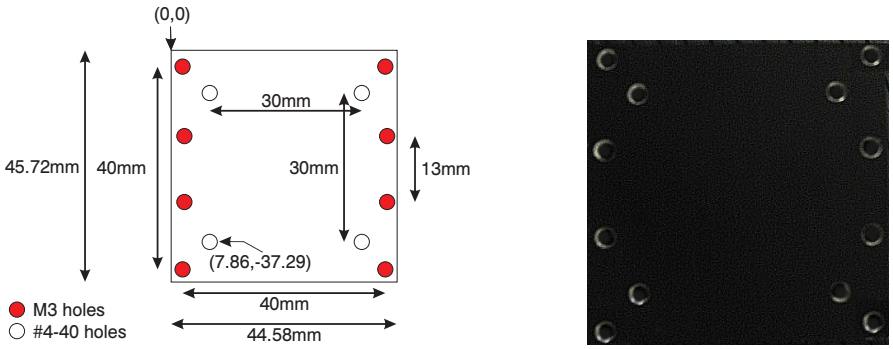

(a) Specifications of the heatsink drill holes.

(b) Picture of the end result.

Figure 68: LED holder CNC drilling.

B Piezo stage program flowchart

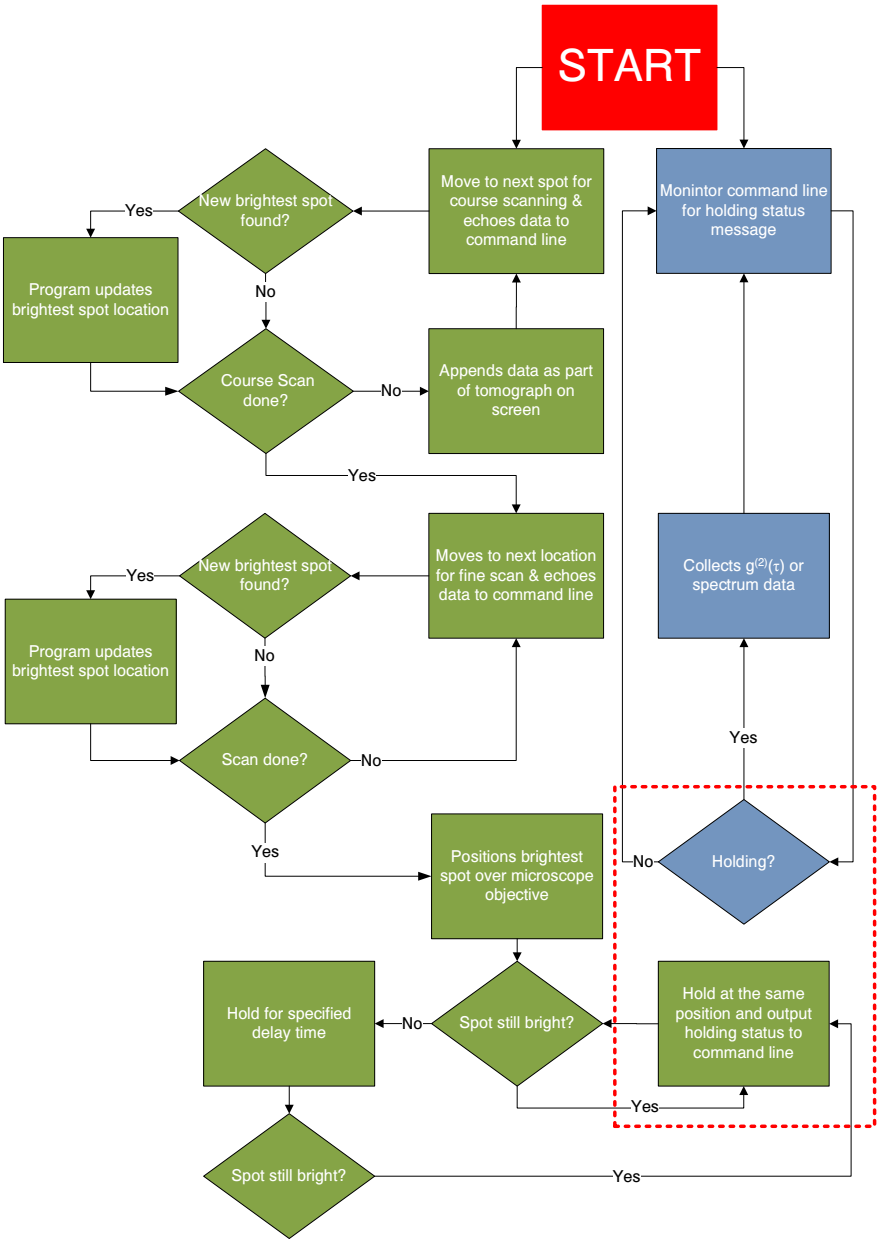

Figure 69: Flow chart depicting the operations of the confocal microscope scanning program. Green colour portion controls the stage and displays information on screen; programmed in Tcl/Tk. Blue colour portions monitor the command line for signs of a single molecule being localized and starts collection of data. Programmed in shell script.

Index

List of Figures

List of Tables

References

[1] Charles H. Bennett and Gilles Brassard. Quantum cryptography: Public key distribution and coin tossing. *Proceedings of the IEEE International Conference on Computers, Systems, and Signal Processing*, page 175, 1984.

[2] Artur K. Ekert. Quantum cryptography based on Bell's theorem. *Phys. Rev. Lett.*, 67(6):661–663, Aug 1991.

[3] Brahim Lounis and Michel Orrit. Single-photon sources. *Reports on Progress in Physics*, 68(5):1129–1179, 2005.

[4] Hans A. Bachor and Timothy C. Ralph. *A Guide to Experiments in Quantum Optics*. Wiley-VCH, 2004.

[5] Alexander Ling, Matt Peloso, Ivan Marcikic, Antía Lamas-Linares, and Christian Kurtsiefer. Experimental E91 quantum key distribution. *Proc. of SPIE*, 6903:69030U–1, 2008.

[6] Eugene Hecht. *Optics*. Addison Wesley, 2002.

[7] Charles Santori, David Fattal, and Jelena Vuckovicand Glenn S. Solomon & Yoshihisa Yamamoto. Indistinguishable photons from a single-photon device. *Nature*, 419:594–597, 2002.

[8] Peng Jin-Sheng and Li Gao-Xiang. *Introduction to Modern Quantum Optics*. World Scientific, 1998.

[9] Brahim Lounis and W.E Moerner. Single photons on demand from a single molecule at room temperature. *Nature*, 407:491–493, Sept 2000.

[10] Christian Kurtsiefer, Sonja Mayer, Patrick Zarda, and Harald Weinfurter. Stable solid-state source of single photons. *Phys. Rev. Lett.*, 85(2):290–293, Jul 2000.

[11] T. Gaebel, I. Popa, A. Gruber, M. Domhan, F. Jelezko, and J. Wrachtrup. Stable single -photon source in the near infrared. *New Journal of Physics*, 6:98, 2004.

[12] Jason S. Kuo, Christopher L. Kuyper, Peter B. Allen, Gina S. Fiorini, and Daniel T. Chiu. High-power blue/UV light-emitting diodes as excitation sources for sensitive detection. *Electrophoresis*, 25:3796–3804, 2004.

[13] M. Unger, E.Kartalov, C.-S. Chiu, H.A. Lester, and S.R. Quake. Single-molecule fluorescence observed with mercury lamp illumination. *BioTechniques*, 27:1008–1014, Nov. 1999.

[14] V. Jacques, J.D Murray, F. Marquier, D. Chauvat, F. Grosshans, F. Treussart, and J.-F. Roch. Enhancing single-molecule photostability by optical feedback from quantum jump detection. *Applied Physics Letters*, 93, Nov. 2008.

[15] W.E. Moerner. Single-photon sources based on single molecules in solids. *New Journal of Physics*, 6:88, 2004.

[16] F. Kulzer, F. Koberling, Th. Christ, A. Mews, and Th. Basch. Terrylene in p-terphenyl: single-molecule experiments at room temperature. *Chemical Physics*, 247(Issue 1):23–34, August 1999.

[17] Bert Hecht and Lukas Novotny. *Principles of Nano-Optics*. Cambridge University Press, 2006.

[18] Brian Herman, Victoria E. Centonze Frohlich, Joseph R. Lakowicz, Douglas B. Murphy, Kenneth R. Spring, and Michael W. Davidson. Olympus microscopy resource center, fluorescence microscopy, basic concepts in fluorescence.

[19] S.P. McGlynn, T. Azumi, and M. Kinoshita. *Molecular Spectroscopy of the triplet state*. Prentice-Hall, 1969.

[20] Christian Florian Seebacher. *Einzelmolekülspektroskopie von organischen Farbstoffmolekülen in porösen Festkörpern und Tieftemperaturspektroskopie an dem grün fluoreszierenden Protein*. PhD thesis, Ludwig-Maximilians-Universität München, 2002.

[21] Oliver Panzer, Wolfgang Ghde, Ulrich C. Fischer, Harald Fuchs, and Klaus Müllen. Influence of oxygen on single molecule blinking. *Advanced materials*, 10(Issue 17):1469–1472, December 1998.

[22] A. Nicolet, M. A. Kol'chenko, B. Kozankiewicz, and M. Orrit. Intermolecular intersystem crossing in single-molecule spectroscopy: Terrylene in anthracene crystal. *The Journal of Chemical Physics*, 124:164711, 2006.

[23] S. Kummer, F. Kulzer, R. Kettner, Th. Basch, C. Tietz, C. Glowatz, and C. Kryschi. Absorption, excitation, and emission spectroscopy of terrylene in p-terphenyl: Bulk measurements and single molecule studies. *The Journal of Chemical Physics*, 107(19):7673–7684, 1997.

[24] R.J. Pfab, J. Zimmermann, C. Hettich, I. Gerhardt, A. Renn, and V. Sandoghdar. Aligned terrylene molecules in a spin-coated ultrathin crystalline film of *p*-terphenyl. *Chemical Physics Letters*, 387:490–495, 2004.

[25] R. Q. Twiss, A. G. Little, and R. Hanbury Brown. Correlation between photons, in coherent beams of light, detected by a coincidence counting technique. *Nature*, 180:324–326, August 1957.

[26] Rodney Loudon. *The quantum theory of light*. Oxford University Press, 3rd edition, 2000.

[27] K Sam Wells, David R. Sandison, James Strickler, and Watt W. Webb. *Quantitative fluorescence imaging with laser scanning confocal microscopy*, chapter 3, pages 27–39. Plenum Press, 1990. Handbook of biological confocal microscopy.

[28] http://www.spachoptics.com/v/vspfiles/photos/uplsapo-100-2t.jpg. Picture.

[29] Maksymilian Pluta. *Advanced Light Micrscopy*, volume 1. Elsevier, 1988.

[30] I. Shinya. *Foundations of confocal scanned imaging in light microscopy*, chapter 1, pages 1–13. Plenum Press, 1990. Handbook of biological confocal microscopy.

[31] http://www.microscopyu.com/tutorials/java/virtual/confocal/.

[32] Commission Internationale de l'Eclairage proceedings. Cie 1931 standard colorimetric observer y2(lambda) data (between 380 nm and 780 nm at 5 nm intervals), 1932.

[33] Jnos Schanda. *Colorimetry: Understanding the CIE system*, chapter 3, pages 25–76. Wiley-Interscience, 2007.

[34] Henri Dautet, Pierre Deschamps, Bruno Dion, Andrew D. MacGregor, Darleene MacSween, Robert J. McIntyre, Claude Trottier, and Paul P. Webb. Photon counting techniques with silicon avalanche photodiodes. *Applied Optics*, 32(No. 21):3894, July 1993.

[35] Perkin-Elmer. Silicon avalanche photodiodes c30902 series technical datasheet.

[36] Bahaa E.A. Saleh and Malvin Carl Teich. *Fundamentals of Photonics*. Wiley-Interscience, 2nd edition edition, 2007.

[37] Max Born and Emil Wolf. *Principles of Optics*. Cambridge University Press, 7th (expanded) edition, 2002.

[38] Richard Young. Measuring light emission from leds. *Advanced LEDs for Solid State Lighting, Proceedings of SPIE*, 6355:63550H–1, 2006.

[39] Daniel Zwillinger. *CRC Standard Mathematical Tables and Formulaes*. CRC Press, Chapham & Hall, 31th edition, 2003.

[40] Edge filter spectra vs. angle of incidence, semrock inc. technical notes.

[41] Andrew H. Fischer, Kenneth A. Jacobson, Jack Rose, and Rolf Zeller. Preparation of slides and coverslips for microscopy. *Cold Spring Habour Protocols*, 2008.